The Meteoritical Society

Meteoritics & Planetary Science 44, Nr 9, 1243–1264 (2009)
Abstract available online at http://meteoritics.org

Penetration tracks in aerogel produced by Al_2O_3 spheres

Friedrich HÖRZ[1*], Mark J. CINTALA[2], Thomas H. SEE[3], and Keiko NAKAMURA-MESSENGER[3]

[1]LZ-Technology Inc./ESCG, Mail Code JE 23, 2224 Bay Area Blvd., Houston, Texas 77058, USA
[2]Astromaterials Research Branch, KR, NASA Johnson Space Center, Houston, Texas 77058, USA
[3]ESCG, Mail Code JE 23, 2224 Bay Area Blvd., Houston, Texas 77058, USA
[*]Corresponding author. E-mail: friedrich.p.horz@nasa.gov

This paper is dedicated to Freiherr Wolf von Engelhardt (1910–2008), a beloved teacher, colleague and friend, and an inspirational beacon to so many of us interested in extraterrestrial materials and the cratering process

(Received 11 August 2008; revision accepted 27 April 2009)

Abstract–We conducted impact experiments into SiO_2-based aerogel of uniform density (0.02 g cm^{-3}) with spherical corundum projectiles. The highly refractory nature and mechanical strength of corundum minimizes projectile deformation and continuous mass loss by ablation that might have affected earlier experiments with soda-lime glass (SLG) impactors into aerogel targets. We find that corundum is a vastly superior penetrator producing tracks a factor of 2.5 longer, yet similar in diameter to those made by SLG. At velocities >4 km s^{-1} a cylindrical "cavity" forms, largely by melting of aerogel. The diameter and length of this cavity increase with velocity and impactor size, and its volume dominates total track volume. A continuously tapering, exceptionally long and slender "stylus" emerges from this cavity and makes up some 80–90% of the total track length; this stylus is characterized by solid-state deformations. Tracks formed below 4 km s^{-1} lack the molten cavity and consist only of a stylus. Projectile residues recovered from a track's terminus substantially resemble the initial impactors at V < 4 km s^{-1}, yet they display two distinct surfaces at higher velocities, such as a blunt, forward face and a well-preserved, hemispherical trailing side; a pronounced, circumferential ridge of compressed and molten aerogel separates these two surfaces. Stringers and patches of melt flow towards the impactor's rear where they accumulate in a characteristic melt tip. SEM-EDS analyses indicate the presence of Al in these melts at velocities as low as 5.2 km s^{-1}, indicating that the melting point of corundum (2054 °C) was exceeded. The thermal model of aerogel impact by Anderson and Cherne (2008) suggests actual aerogel temperatures >5000 K at comparable conditions. We therefore propose that projectile melting occurs predominantly at those surfaces that are in contact with this very hot aerogel, at the expense of viscous heating and associated ablation. Exposure to superheated aerogel may be viewed as extreme form of "flash heating." This seems consistent with observations from the Stardust mission to comet Wild 2, such as relatively pristine interiors of rather large, terminal particles, yet total melting of most fine-grained dust components.

INTRODUCTION

A number of impact experiments into highly porous, low-density, SiO_2-based aerogel have been conducted in the past as summarized by Burchell et al. (2006). Most of these efforts concentrated on demonstrating that the modest peak stresses generated during hypervelocity impact with such low-density media are insufficient to melt typical geologic solids, as first demonstrated by Barrett et al. (1992) and most recently by Noguchi et al. (2007). These observations suggested that unmolten residues of interplanetary dust particles might be captured in low Earth orbit (e.g., Hörz et al. 2000) or on sample return missions such as Stardust to comet P/81 Wild 2 (e.g., Tsou et al. 2003; Brownlee et al. 2006). Given its optically transparent nature, SiO_2-based aerogel became the medium of choice for cosmic dust collectors, replacing substantially opaque polymer foams (e.g., Tsou 1990) and other porous media employed in the "soft" capture of high-velocity crater ejecta or explosion products (e.g., Gratz et al. 1993). Collector transparency is critical in locating the projectile residue, typically <50 μm in size, at the track's terminus for in situ analyses and/or extraction from the collector (e.g., Westphal et al. 2004).

Despite substantial progress on the phenomenology of

aerogel tracks and associated particle capture during the last decade, the mechanical and thermodynamic processes during high-speed aerogel penetration remain poorly understood. Projectile deceleration is accomplished through a complex combination of shock processes, a formidable problem in itself for highly porous media (e.g., Ahrens and Cole 1974), and viscous drag (Anderson and Ahrens 1994; Trucano and Grady 1995; Dominguez et al. 2004; Trigo-Rodríguez et al. 2008). Current modeling attempts are not possible without major assumptions regarding thermodynamic material constants at elevated pressures and other physical properties of aerogel, including its crushing strength under dynamic conditions. An especially critical and challenging aspect relates to the detailed pressure-temperature histories of the recovered projectile residues. Obviously, any mineralogical or compositional modification during the capture process must be understood to deduce the texture, mineralogy, composition, and other properties of the pristine impactors and their astrophysical source(s).

This is especially true for the Stardust mission, the most significant scientific application of aerogel soft capture to date, which employed density-graded aerogel, ranging from 0.005 g cm^{-3} at the surface to some 0.05 g cm^{-3} at the final collector depth of 30 mm (Tsou et al. 2003). Additionally, the impactor materials varied greatly on Stardust from non-porous, monomineralic grains such as olivine to loosely consolidated, most likely highly porous, friable aggregates of poorly known yet generally low densities (<1 g cm^{-3}; e.g., Zolensky et al. 2006). As a consequence of this large diversity in impactor properties, a wide variety of track morphologies was observed in the Stardust collectors (e.g., Hörz et al. 2006 or Burchell et al. 2008), and the pressure-temperature (*P*-*T*) conditions for the harvested residues range from melting of the finest fractions to the survival of large, seemingly pristine, monomineralic grains (Brownlee et al. 2006; Zolensky et al. 2006; Ishii et al. 2008a, 2008b; Keller and Messenger 2008).

To advance a first-order theoretical understanding of aerogel penetration, we conducted impact experiments under somewhat idealized conditions attempting to minimize some of the complications inherent in most of the earlier experiments. First, we employed monolithic aerogels of lower density (0.02 g cm^{-3}) than the most systematic study to date on such targets (>0.06 g cm^{-3}; Burchell et al. 2001); using aerogel of constant density obviously avoids the complexities arising from the density-graded materials that were employed by Stardust (Burchell et al. 2008). Second, we used polycrystalline Al_2O_3 (α-corundum) spheres as impactors. The thermodynamic properties of Al_2O_3 are better defined than those of soda-lime glass (SLG) which was used in most earlier studies; the refractory nature of Al_2O_3 should also minimize ablation and continuous mass loss during penetration (see Anderson and Ahrens 1994). Additionally, Al_2O_3 has higher compressive and tensile strengths compared to typical silicates and it will thus minimize, and possibly eliminate potential impactor deformation, including fragmentation, by the initial shock (see Trucano and Grady 1995). While somewhat removed from understanding the penetration of natural objects, these simplified experimental conditions may be viewed as end-member cases to understand the penetration phenomena in aerogel. Obviously, this baseline must be expanded in the future by the incremental introduction of complicating factors, such as impactors with lower melting points, other densities or physical strengths, and/or more complex targets.

IMPACT EXPERIMENTS

The experiments were conducted with a 5 mm light gas gun that is described in http://ares.jsc.nasa.gov/education/websites/craters/gunlabtour.htm (02/11/2009). All projectiles were <100 μm in diameter and "shot gunned" via a four-piece, serrated sabot, while the gun was evacuated to 0.1 to 0.15 mbar. The velocity of the sabot pieces was measured by four laser photodiode stations; additionally, a photodiode detected the light flash upon impact. Agreement between the flash detector and laser stations was better than 1%; the duration of the light pulse, indicative of successive impacts, suggested a velocity dispersion of the incoming projectile cloud of <5%, typically <3%.

The aerogel targets were manufactured by P. Tsou (Jet Propulsion Laboratory) and possessed a nominal density of 0.02 g cm^{-3}; our own measurements on five samples ranged from 0.019 to 0.024 g cm^{-3}. These materials were part of the Orbital Debris Capture (ODC) experiment, an attached payload on the Mir station in low Earth orbit (Hörz et al. 2000). ODC consisted of 72 aerogel tiles, each 10 cm on a side, and 1 cm deep. Only about 40% of those tiles were consumed during post-mission analysis and we selected four from those remaining for the present experiments. The physical appearance (transparency, color, etc.) of the space-exposed tiles was indistinguishable from unexposed materials. Quantitative measurements regarding physical properties, however, are not available on either unexposed or space-exposed specimens. We therefore duplicated an earlier experiment that used unexposed ODC aerogel (Hörz et al. 1998) with a space-exposed ODC tile and 50 μm diameter SLG projectiles at an impact velocity of 5.1 km s^{-1}; we found no differences in track length or overall track morphology in the space-exposed target compared to the unexposed specimen used in the earlier experiments.

Each tile was cut in half with a wire saw to produce 5 × 10 × 1 cm samples which were further subdivided into 5 × 2 × 1 cm blocks using a small diamond blade saw, modified in house for cutting aerogel. Each experiment employed two of these pieces, placed next to each other inside a snug, thin-walled cardboard box; this allowed for a maximum penetration depth of 5 cm and produced a target surface of

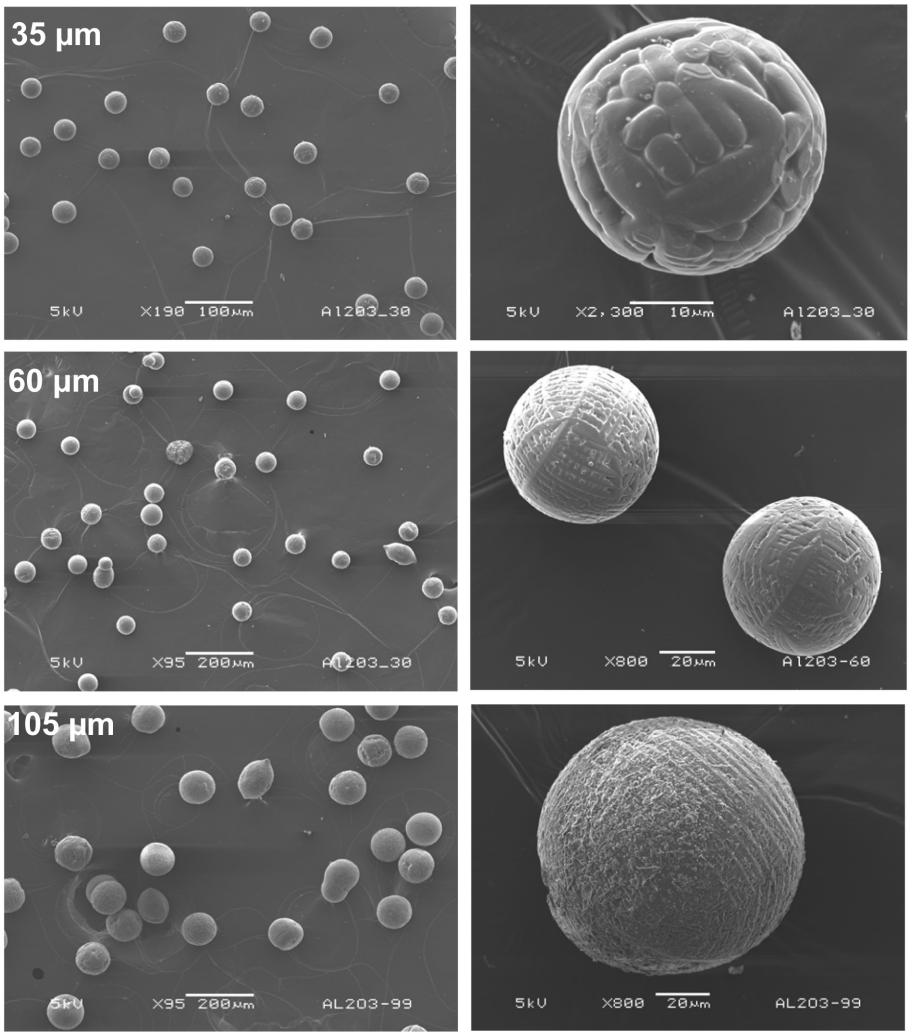

Fig. 1. Representative images of the α-corundum projectiles used in this study illustrating the distribution of relative sizes and shapes, as well as their polycrystalline nature and associated surface textures.

approximately 2 × 2 cm. The 100 µm projectiles mandated the use of two wire-cut halves to accommodate penetration depths >5 cm. Only those tracks that were completely confined to one of the two target blocks were analyzed; rare tracks close to the (vertical) interface of the slabs, affecting or damaging both, were rejected for analysis.

The projectiles (from Microspheres-Nanospheres, Cold Spring, NY) were spheres of polycrystalline α-corundum, nominally pure Al_2O_3 of density 3.97 g cm^{-3} and in sizes of 35, 60, and 105 µm, as illustrated in Fig. 1. Our own SEM analyses revealed the size distributions of Fig. 2a, with the average projectile diameter (D_p) defined as the mean of 3 to 4 measurements per sphere, the latter including maximum (D_{pmax}) and minimum (D_{pmin}) diameters. The 60 and 105 µm fractions contained progressively larger proportions of oblong spheroids as shown in Fig. 2b. Based on these observations, some 5–10% of individual projectiles in the 60 and 105 µm fractions could have had masses as much as a factor of 2 to 3 larger than the nominal particle defined by the mean diameter in Fig. 2a. It is also important to note that the polycrystalline spheres display substantial surface detail in the form of individual crystal faces as illustrated by the enlarged images of Fig. 1. This totally fortuitous and ubiquitous surface texture may potentially be useful in evaluating whether a projectile's surface underwent melting or not.

Consistent with the overall objectives of this study, we launched projectiles of all three sizes at a constant velocity, nominally 6.1 km s^{-1}, thus duplicating the Stardust conditions. We also experimented with variable velocity (from 3 to 6 km s^{-1}) at constant impactor size, selecting the 60 µm spheres for that purpose. This simple experimental matrix was designed to separate the effects of impactor size and velocity.

Following an experiment, the samples were observed and photographed using diverse optical microscopes. The track dimensions were measured with a compound microscope (Olympus BX60) that possessed a calibrated X/Y scanning table. Harvesting of individual projectile residues was

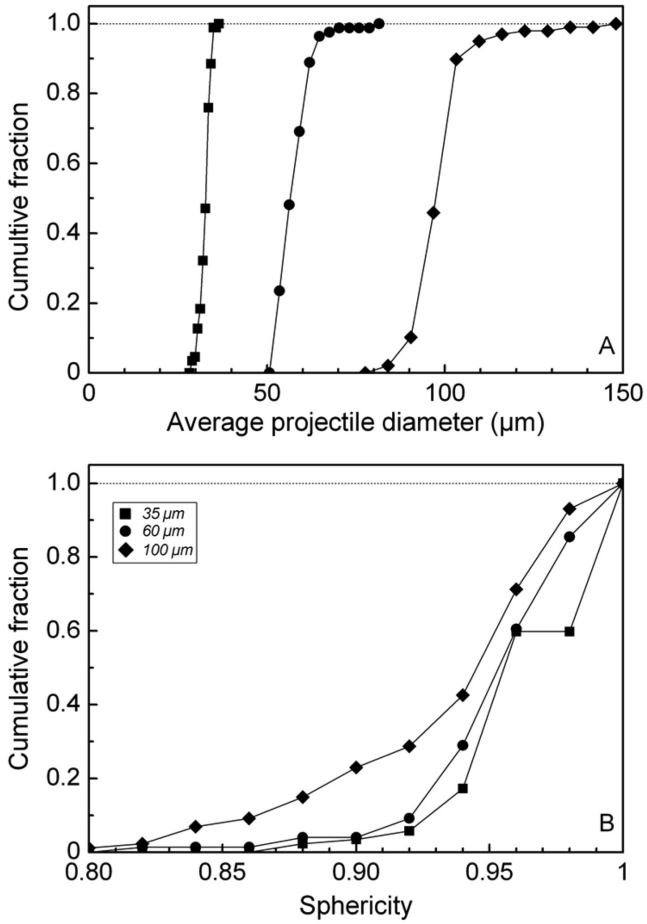

Fig. 2. A) Cumulative size distributions of the projectiles. B) Cumulative distribution of projectile sphericities (D_{min}/D_{max}). Note that the 60 and 100 μm size fractions contain some 8% and 20% particles of <0.90 sphericity, respectively, mostly in the form of dumbbell-shaped objects, that manifest themselves as unusually large average diameters in (A).

accomplished with needles under a binocular microscope following the procedures developed for Stardust; the pristine and recovered projectiles were imaged in JSC's JEOL 5910LV scanning electron microscope.

TRACK MORPHOLOGY

Overview

Without exception, all tracks in the 0.02 g cm^{-3} aerogel made by corundum projectiles were exceptionally slender compared to those of SLG spheres in a variety of aerogels (Hörz et al. 1998; Burchell et al. 2001, 2008). Several examples of entire target blocks are illustrated in Fig. 3, illuminating the gross morphology of the Al_2O_3 tracks and their reproducibility. Their spatial density was designed to be high (by loading large numbers of projectiles into the sabot) to have a large number of tracks per experiment. Unfortunately, this approach adversely affects the photo-documentation of individual blocks, as many tracks project on top of others and limitations of the microscope's focal depth render many tracks out of focus. Also, the overviews presented in Fig. 3 do not faithfully capture the termini of tracks as they were too faint and/or out of focus. Figure 3, nevertheless, serves to illustrate that there is substantial scatter in track lengths for each experiment, which will be detailed later. This is a somewhat annoying situation in all aerogel experiments using small, shot-gunned projectiles (e.g., Hörz et al. 1998; Burchell et al. 2001), because it is simply not possible to control total impactor mass precisely, given the size distribution and shape factors of the initial projectile population. Very short tracks are most likely produced by gun debris or by flawed projectiles that broke up upon launch. Nevertheless, it is easy to associate the dominant track population with the nominal impactors.

Figure 4 illustrates a single track, typical for 60 μm spheres at 6.04 km s^{-1}, while Fig. 5 is at 3.1 km s^{-1} under otherwise identical conditions. Following Hörz et al. (1998), a track begins with the *entrance hole*, followed by a paraboloidal section (the *throat)*, until *maximum cavity diameter* is reached (at point *L1* in Fig. 4). The *main cavity* extends to some depth (e.g. *L2* in Fig. 4), beyond which we observe a continuously tapering *stylus* that extends all the way to the *projectile residue* at the track's *terminus.*

Entrance Hole

The entrance hole is difficult to observe optically due to interference by subsurface damage in the highly transparent aerogel as noted by many (e.g., Burchell et al. 2001, 2006, 2008). We attempted to eliminate some of these difficulties by sawing thin (~1 mm thick) wafers parallel to the target surface, thus physically removing much of the undesirable subsurface fractures. Figure 6 provides a summary of our experiments. Figures 6h and i are from a thick, unprocessed target and illuminate the effects of the subsurface damage; the actual entrance holes are barely discernible. All other images are from thin slices and show marked improvement in the definition of entrance holes. Nevertheless, all entrance holes at impact speeds >5 km s^{-1} are highly irregular in plan view and differ easily in size by a factor of two in a given experiment. The actual target surface is modestly depressed around the entrance hole and there is no evidence for surface spallation, the typical response of brittle targets. The irregular holes are entirely due to undercutting from below as the cavity expands radially. Presumably, the aerogel is compressed during the actual impact and fails in tension during the ensuing decompression. The original entrance hole is in most cases completely dislodged by this undercutting and the latter produces an irregular hole with rather jagged edges. These edges are made up of exceedingly thin, wedge-shaped slivers that are easily dislodged, even during careful

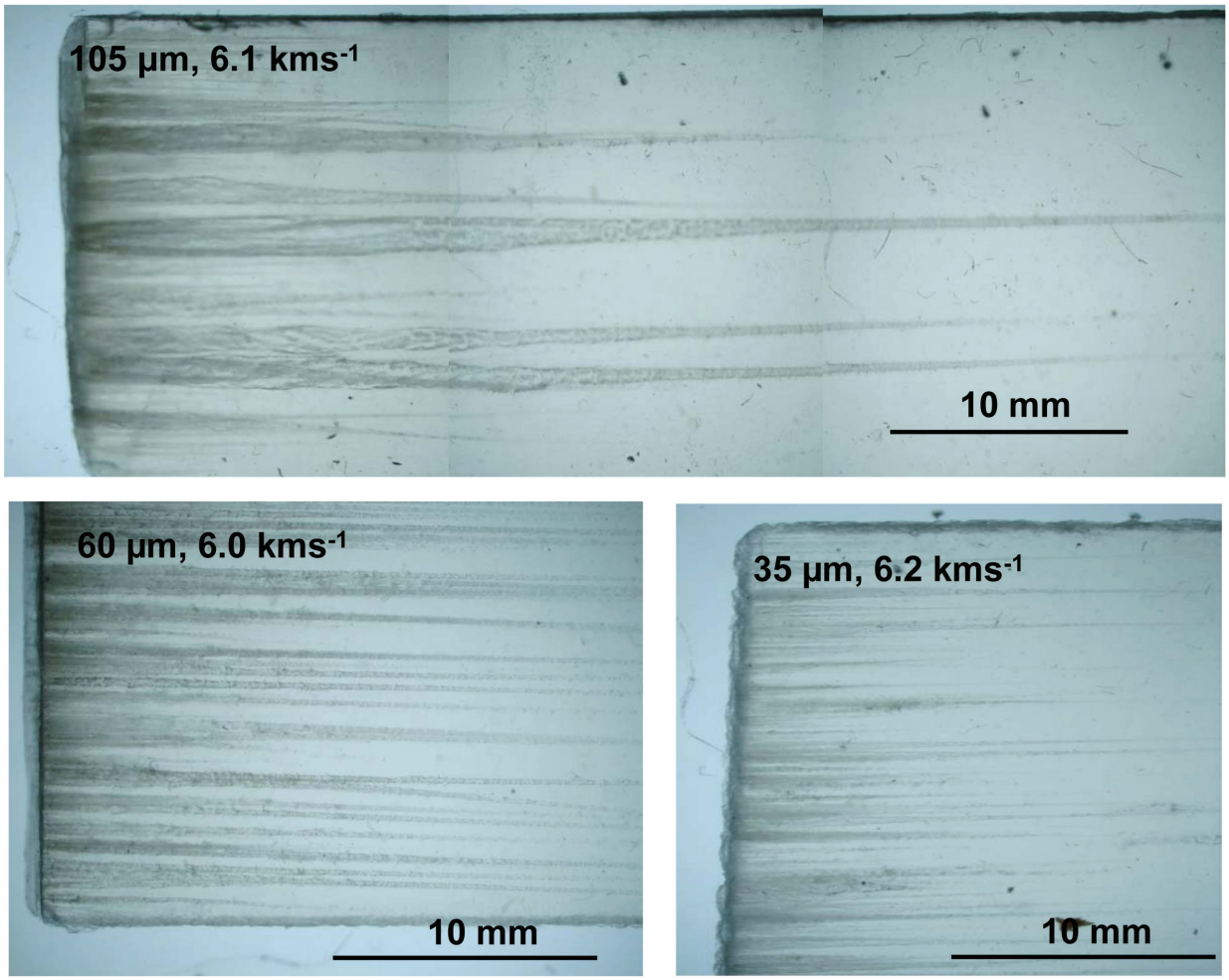

Fig. 3. Overviews of aerogel targets impacted by Al_2O_3 spheres with diameters of 105, 60, and 35 µm, all at some 6 km s^{-1}.

post-event handling of the targets. In contrast, tracks from the low-velocity experiments (<3.6 km s^{-1}) lack the pervasive undercutting, thus preserving the actual entrance hole (see Figs. 6a–d). A typical low-velocity entrance hole also has a distinct "lip" of unbroken aerogel that differs diagnostically from the jagged, fragmented edges at high velocities. Burchell et al. (2001) classified round entrance holes (a–d) as Type I, nearly circular holes with radial cracks as Type II (e.g., l and m) and irregular holes as Type III; we concur with this classification and the earlier observations that the transition of the various types is gradational.

We have measured the average hole diameter (D_E), typically with 3–5 measurements per hole, and find that D_E = 1.2 D_p and 2.0 D_p at 3.1 and 3.6 km s^{-1}, respectively, and around 4–6 D_p at V >5.2 km s^{-1}, the latter consistent with Burchell et al. (2008) for SLG projectiles into Stardust aerogel. The relationships at the high velocities, however, should be used with some caution in deducing projectile sizes for individual tracks as hole diameter can easily vary by a factor of two under otherwise identical impact conditions, and thus by a factor of 8 in impactor mass.

Throat and Main Cavity

Details of characteristic throat and cavity features for 60 µm/6 km s^{-1} tracks are shown in Fig. 7. A highlight of the stereomicroscope image of Fig.7a is the undulating surface relief of both the throat and main cavity. Modest ridges and valleys combine into a network of distinctly twisted appearance. Individual twists rarely rotate more than 120° around the track axis and none combine into complete 360° spirals. Figure 7a also shows that the crests of individual promontories are invariably peppered by particulates that scatter the incident light; the swales or valleys are distinctly transparent in comparison. Figures 7b and c, taken in transmitted light, not only illustrate additional examples of paraboloidal throats, but they also illuminate the dichotomy in surface texture between smooth, transparent portions of the cavity walls and those decorated by trails of particulates. Fig. 7d is a partial enlargement of Fig. 4, and illustrates the intricate networking and twisting of these particulate trails.

The interior cavity walls were investigated by SEM, as shown in Fig. 8. Figure 8a depicts a 60 µm/6 km s^{-1} track

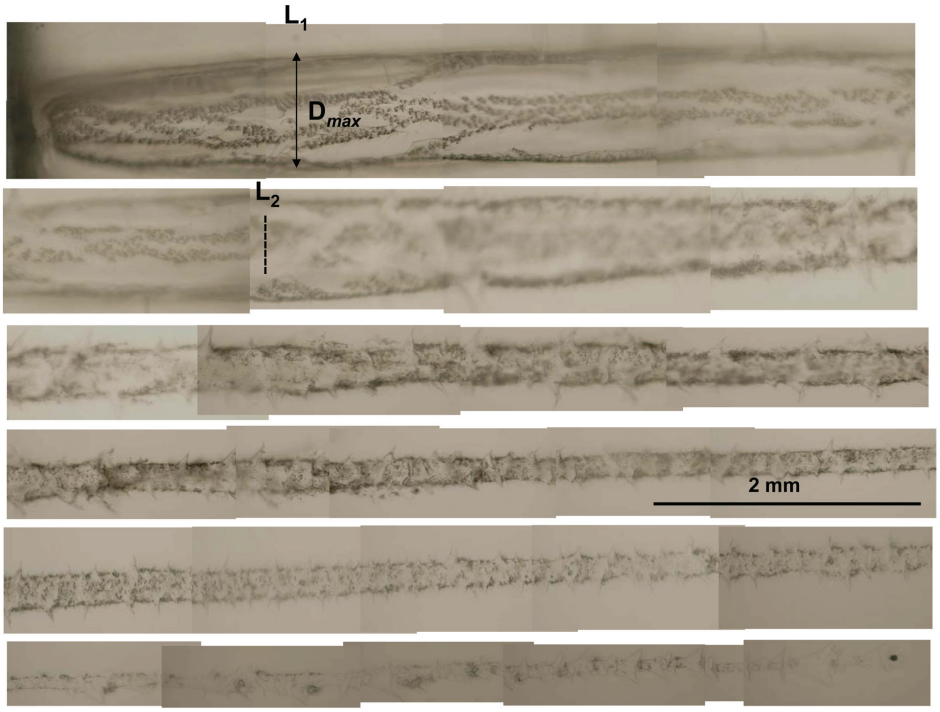

Fig. 4. Typical track made by a 60 µm corundum projectile at 6 km s^{-1}. See text for details.

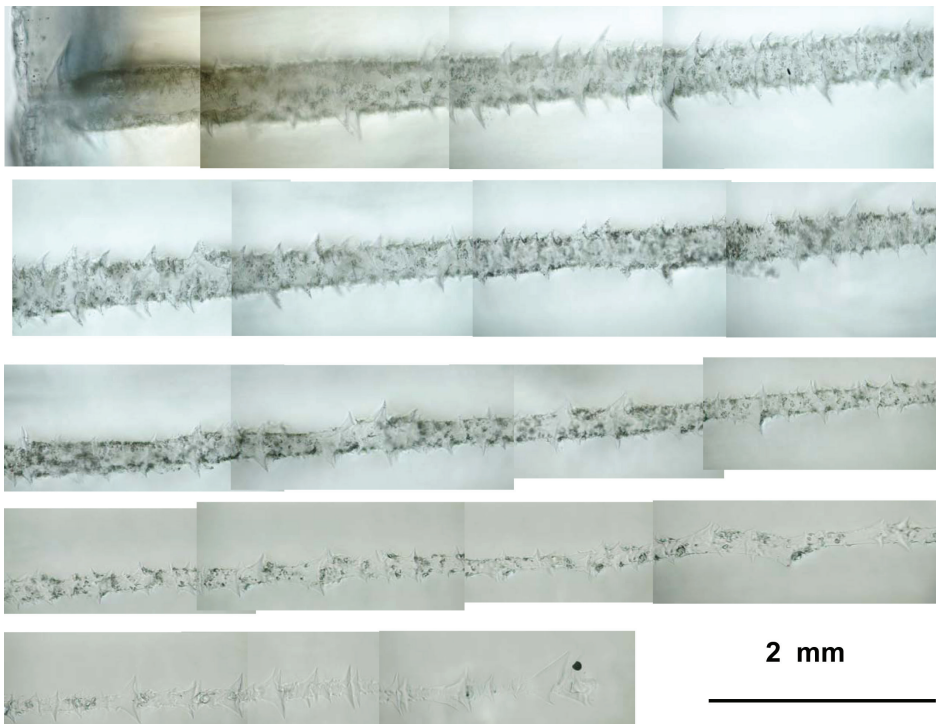

Fig. 5. Overview of a single track produced by a 60 µm corundum projectile at 3.1 km s^{-1}. See text for details.

which was bisected with a razor blade; the pervasive fracturing seen in this image occurred during this procedure. Nevertheless, individual trails of particulates are readily discerned. Successively higher magnifications (Figs. 8b–d) reveal clusters and clumps of fine-grained material, some of which is rounded and occasionally even spherical (Fig. 8d). Thus, the trails are composed of rather fine-grained clumps of solid (and compressed?) aerogel, intimately mixed with

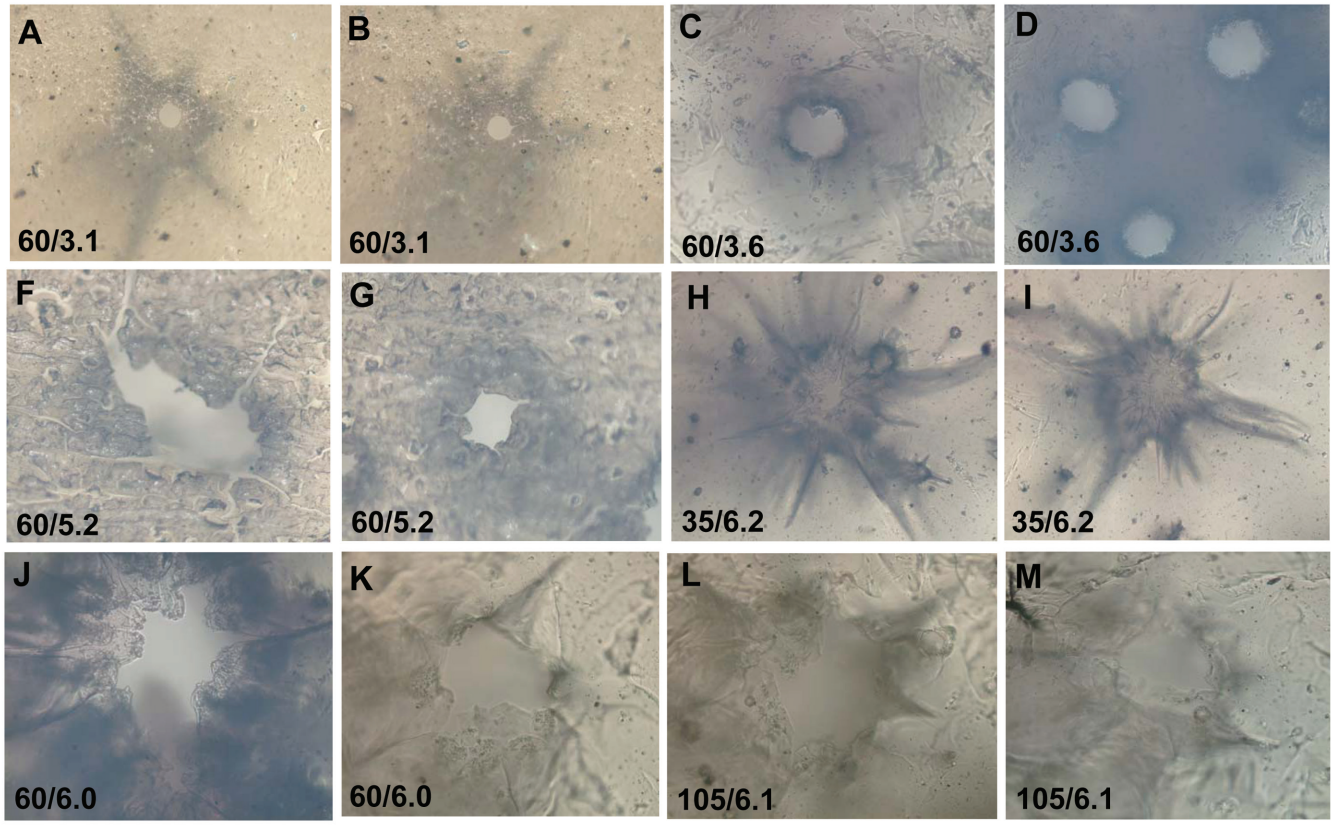

Fig. 6. Representative entrance holes with projectile size and impact velocity indicated in lower left-hand corner. a–d) Low-velocity experiments producing relatively round, regular entrance holes. f–m) High-velocity experiments resulting in rather irregular entrance holes.

aerogel melts. The exact nature of the smooth cavity walls is difficult to evaluate due to the pronounced fracturing introduced during sample preparation. Nevertheless, note that the particulate trails reside on a substrate that occasionally dislodged in distinctly platy fashion, as if it were a thin, competent layer. We interpret the latter as a thin liner of aerogel melt. Molten cavity walls also seem supported by what appear to be schlieren in the optical microscope (see Figs. 7c–d). Furthermore, there is no sign of fractures or other deformation features in the immediate vicinity of the track walls in marked contrast to the stylus (see below). Cavity formation and the early penetration process seem characterized by aerogel melting which subsequently transitions to solid-state processes when the stylus emerges from the cavity.

Returning to details of the cavity walls, we have observed similar undulatory surfaces and associated swirls of particulates in earlier aerogel experiments using SLG projectiles (Fig. 4 in Hörz et al. 1998). They also occur, albeit rarely, in the space-exposed ODC collectors (Hörz et al. 2000). Additionally, two Stardust features display "spiral" trails of particulates as observed by one of us (K. N-M). Detailed X-ray tomography and associated 3D reconstruction of both tracks by Tsuchiyama and Iida (2007) revealed that these spirals are not continuous, but are instead confined to a specific side of each track; nevertheless, the Stardust features twist more severely than any of our experimental tracks.

The origin and significance of these features remains enigmatic. They are common in the present experiments above 4 km s^{-1}, but they are starkly absent in the 3.1 and 3.6 km s^{-1} tests. Thus, they exhibit a velocity dependence. However, neither the encounter velocity of Stardust (6.1 km s^{-1}), nor the much higher velocities for the Earth-orbiting ODC experiment (~15 km s^{-1} on average) produced such features in abundance. This suggests that they might also depend on projectile density which defines, together with impact speed, the peak shock stress at the projectile/target interface. The present experiments employed impactors of 3.97 g cm^{-3}; SLG has a density of 2.4 g cm^{-3} and the majority of ODC and Stardust impactors had lower densities still. Undoubtedly, the present Al_2O_3 projectiles produced the highest shock pressures of all the experimental studies to date, and certainly higher than those of Stardust; however the pressure on the Earth orbiting ODC should be higher than both, due to the elevated encounter speed.

We speculate, therefore, that pressures substantially above the onset of melting, capable to melt large quantities of aerogel, are needed to produce these spirals. This pressure range might not have been reached during most Stardust collisions because of the low-density impactors, and too much

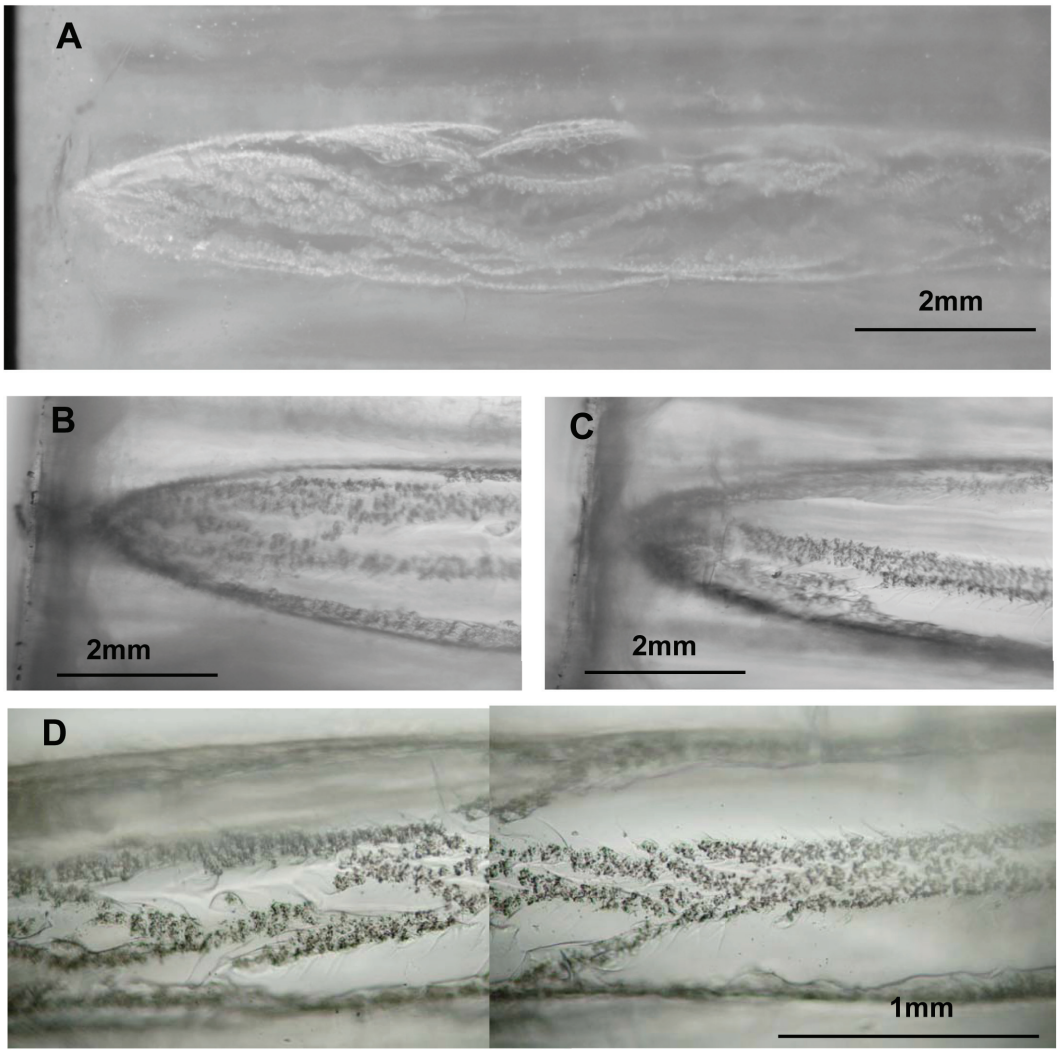

Fig. 7. Main cavities of tracks produced by 60 μm particles impacting at 6 km s^{-1}. a) Oblique illumination under binocular microscope emphasizing the cavity surfaces; note the twisting network of local ridges and swales. b and c) Compound microscope (transmitted light) images of two additional tracks showing the particulate nature of individual ridges and the conical throat. d) Enlargement of the cavity illustrated in Fig. 4, illustrating the networked trails of particulates, and their typically clumped nature. Also note in b–d the large surface portions of perfectly transparent cavity walls, presumably due to the presence of molten aerogel. Where visible in cross section (e.g., b and d), the transparent walls display sharp contacts with the surrounding aerogel, suggesting very little mechanical deformation beyond the actual cavity walls.

melt might have been generated by most ODC impacts because of the high encounter speeds. If this were correct, the presence of twisting and spiraling particulate trails could possibly constrain projectile density and/or velocity.

In principle, all natural or experimental impactors may be rotating, thus imparting some poorly understood, rotational geometry to the ensuing shock. However, unrealistic rotation rates of $>10^7$ rpm would be implied if the twists and spirals directly reflected the impactor's actual spin rate (e.g., a 180° twist over a penetration depth of 1 mm at 6 km s^{-1} results in a rotation rate of 1.8×10^8 rpm that would exceed the tensile strength of any solid). As a consequence, the twists and spirals might merely be initiated by a rotating impactor but they can not be related to its actual spin rate.

Stylus

The essentially linear decrease in track diameter past the main cavity defines the stylus and is invariably marked by the appearance of spike-like fractures. This stylus dominates our standard track at 6 km s^{-1}, comprising some 80% of the total penetration depth (L_T), and it constitutes the entire track at 3 km s^{-1} (Fig. 5). The stylus is thus the dominant feature of aerogel deformation at modest penetration speeds. Figure 9 is from the 60 μm/5.2 km s^{-1} experiment and shows three tracks (all in the microscope's focal plane) at depths of about 0.4 L_T and 0.7 L_T. The typical *spikes* are bounded by a fracture orthogonal to the axis of penetration and another fracture inclined at ~45° which gives them a quasi-conical

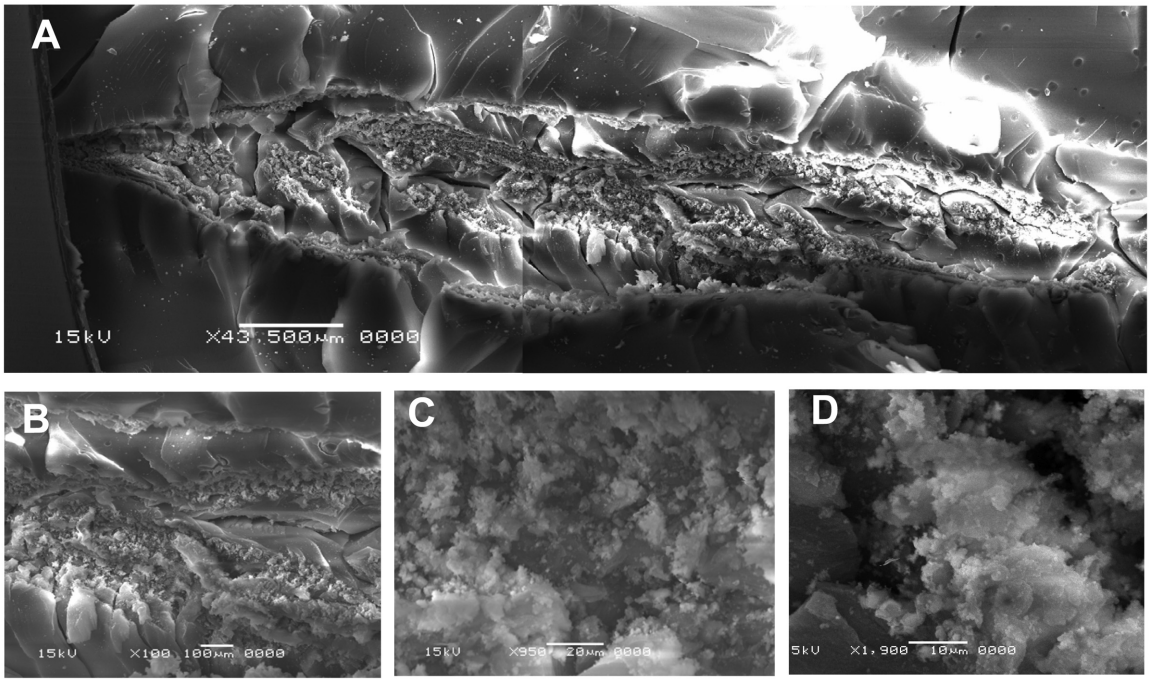

Fig. 8. SEM images of the interior of a 60 µm/6 km s^{-1} cavity that was split open with a razor blade. a) Compare with Fig. 7d and note that most major fractures were introduced during sample preparation. The cavity walls are continuous and seemingly strong, because glassy. Indeed the presence of a competent glass liner is suggested in a few areas where parts of the interior wall plugged during sample preparation. Progressively higher magnifications of the particulate trails are shown in Figs. b–d, illustrating the clumped nature of very fine-grained debris (b, c), and the presence of small, rounded melt droplets (d).

appearance, with the cone's apex invariably pointing up range, towards the surface. Individual spikes occur on either side of the stylus but have no counterparts on the other side. This suggests that they are *partial cones* only, because their base is not a complete circle of 360° azimuth. This renders the spikes diagnostically different from complete *cones* that occur in the tracks' terminal portions (see below).

Figure 10 illustrates near-surface sections of additional tracks from the 3.1 km s^{-1} experiment, all beginning with one giant, cone-shaped fracture immediately below the surface. Also note the absence of any bulbous cavity, which is typical for all tracks <4 km s^{-1}. All penetrations at 3.1 and 3.6 km s^{-1} extend to the terminus as spike-studded, continuously tapering tracks that are identical to those emanating from the main cavity at >5 km s^{-1}. These observations identify the spikes as solid-state deformation features, most likely by tensile failure and tearing of aerogel as suggested by their modestly curved tips.

Spike formation begins when cavity growth by melt-dominated processes stops. The speed of the penetrator at this specific point will thus correspond to the transition from melting to solid state effects; we estimate this speed to be about 4 km s^{-1} based on our 3.6 and 5.2 km s^{-1} shots.

Spike formation continues along most of the ensuing penetration, suggesting that it is typical for a wide range of dynamic conditions, including those under relatively benign stresses at near-terminal velocities. The size of the most prominent spikes decreases with increasing penetration depth and seems proportional to the (decreasing) diameter of the stylus; absolute frequency of the spikes stays relatively constant with depth. Additional analyses are planned to determine these relationships more quantitatively and to evaluate their potential for determining a projectile deceleration profile; unfortunately, only a single datum can be extracted currently for the transition from cavity to stylus at some 4 km s^{-1}.

Terminus

We now turn to the terminal portions (>0.9 L_T) of our experimental tracks as illustrated in Fig. 11. We define this terminal section to coincide with the appearance of fractures perpendicular to the axis of penetration that extend to either side of the track, possessing complete, circular bases to form *complete cones*. The transition form spikes to cones is gradual as illustrated by a mixture of both at around 0.9 L_T and by the progressive development of more cones with depth until they dominate the final sections of a track, almost to the exclusion of spikes. Absolute cone size is highly variable, yet small and large cones alternate systematically along the axis of penetration. Groups of small cones alternate with major cones at a remarkably constant spacing, as if periodic (best seen in the middle panels of Fig. 11). Again, one gains the impression that the dominant, cone-shaped

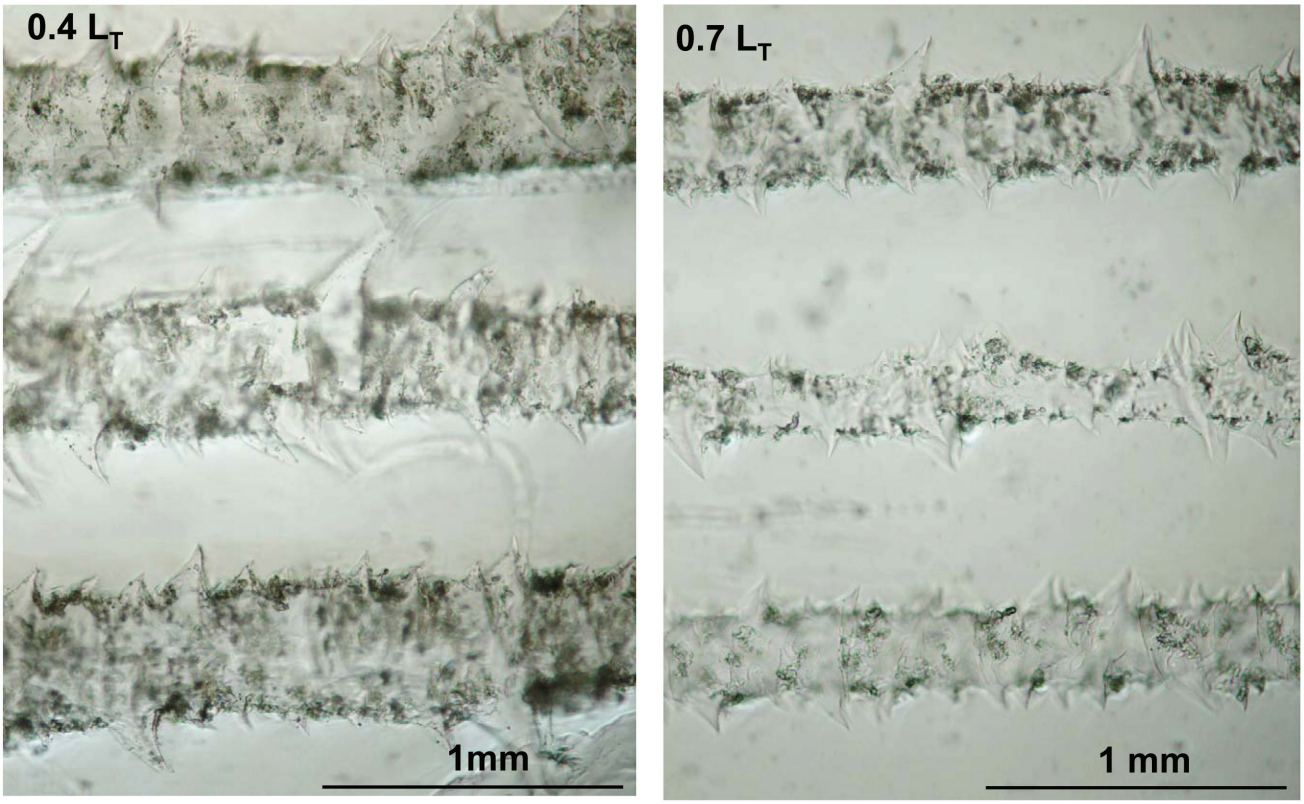

Fig. 9. Stylus details of three tracks, produced by 60 μm projectiles at 6 km s^{-1}, that were fortuitously located within the focal plane of the microscope. These images cover depths of approximately 0.4 L_T (left) and 0.6 L_T. (right). Note the spike-like fractures and their decreasing sizes with increasing penetration depth. Also note the numerous dark spots, most likely compressed aerogel, that occur essentially all along the stylus, rendering the latter distinctly more opaque than either the main cavity or the terminal track sections.

fractures are consistent with tearing, as suggested by their curved tips.

This highly systematic mode of aerogel failure is distinct and characterizes all aerogel tracks in the vicinity of the terminal projectile residue, no matter what initial impact speed. We have no good explanation for the formation of either partial or complete cones, or for the regular, quasi-periodic sequencing of large and small cones. Given the low penetration velocities near the track's terminus, they obviously formed at low stress levels, yet they may still be indicative of high strain rates.

We also observe that the stylus becomes progressively more transparent towards the terminal sections and as the spike features are being replaced by complete cones. We are certain that the numerous dark spots responsible for the opaque nature of the spike-dominated stylus are unrelated to projectile residues, whether fragments or melt droplets (see below), yet we are not sure what these light scatterers really are. They could be tiny droplets of aerogel melt dragged down from higher track portions, particulates of compressed aerogel, or simply tiny fractures or other defects in the aerogel. We prefer solid-state deformations over melt processes for these dark spots because they are so prominent in all low-velocity tracks as well. Clearly, the number of dark spots decreases with decreasing depth and they become virtually absent in the final portions of the track which, as a result, become progressively and remarkably transparent.

The actual termini are presented for a number of tracks in Fig. 12. Figures 12 a–c illustrate tracks at constant impactor size (60 μm) and variable impact velocity, while Figs. 12 d–f reflect variable projectile sizes at constant speed (near 6 km s^{-1}). The termini of all tracks are grossly similar in appearance and no diagnostic information about the initial impact conditions is retained. Each terminus has idiosyncratic details that can include modest curving and misalignment of the last cone (or the last few cones) from the track axis. The projectile residue is typically off axis as well.

Projectile Residues

We extracted representative projectile residues from all experiments, imaged them in the SEM, and conducted qualitative compositional surveys via energy dispersive X-ray spectroscopy (EDS) of their common surface deposits. The only elements of interest were Si and Al, derived from the aerogel and the impactors, respectively. Figure 13 illustrates projectiles from the 60 μm/3.1 km s^{-1} experiment. Their well-preserved surface texture (see Fig.1) identifies these residues

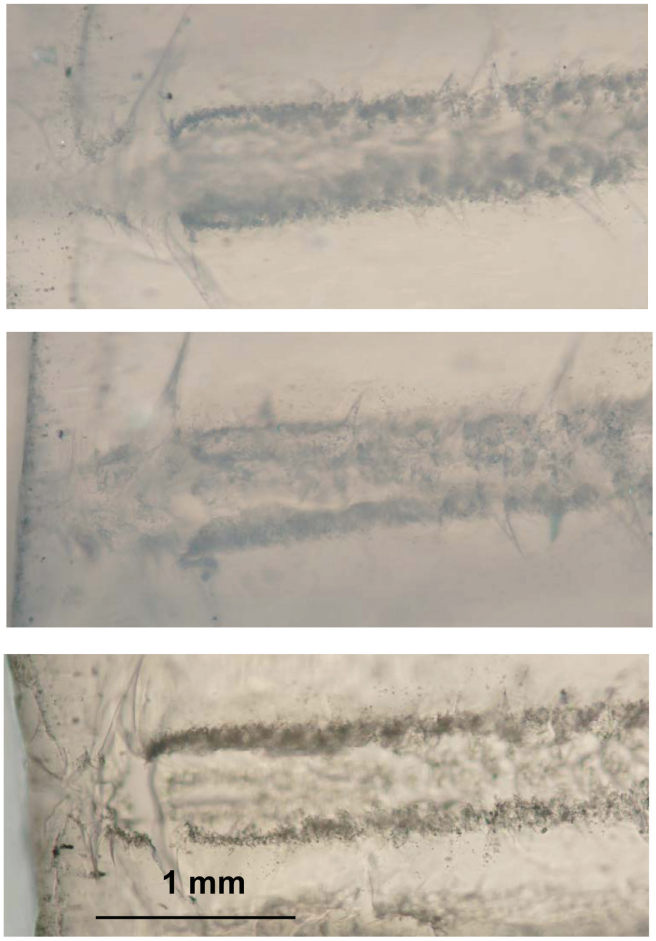

Fig. 10. Representative near-surface portions of tracks produced by 60 μm projectiles impacting at 3.1 km s^{-1}. Note that these low-velocity tracks display a single, fracture near the surface, possess no main cavity, and otherwise resemble the stylus of a typical high-velocity track (see also Fig. 5).

as essentially pristine and unaffected by the capture process. On occasion, some small patches of aerogel, verified by EDS, adhere to their surfaces (e.g., Figs. 13c and 13d); the lack of flow features and droplets suggests that this material is merely compressed, rather than molten aerogel.

Figures 14a–e illustrate five terminal particles from the 60 μm/6 km s^{-1} experiment. Each residue is characterized by a blunt, relatively flat face and an antipodal, quasi-spherical, smooth surface that lacks any of the initial, polycrystalline surface texture. A distinct ridge separates the blunt face from the spherical portions; this ridge is continuous around the entire circumference of the impactor. It is this ridge that gives the residues a somewhat faceted appearance in the optical microscope (see Fig. 12).

EDS reveals that the ridge is composed of Si only; the major melt stringers emanating from the ridge (e.g., Fig. 14f) also yield only Si. Judging from the smooth, knobby surface of the ridge and associated stringers of melt, we interpret this ridge and major stringers to consist of fused aerogel. Figures 14 a–d also reveal small patches and droplets of melts on an otherwise smooth host surface that are distinctly lineated, suggesting melt flow away from the ridge, identical to the large stringers, and toward the trailing edge of the sphere where it accumulates in a distinct, conical tip (Figs. 15a, 15c, and 15d). EDS reveals that the isolated melt patches and droplets on the sphere's surface are dominated by aerogel melts, yet mixtures of Si and Al are present as well; indeed, Al-dominated melts are observed, but some of them may be thin enough to permit fluorescence from the underlying substrate. The massive melt deposits in the conical tip avoid this analytical problem and reveal ubiquitous Al, albeit in highly variable proportions relative to Si. There is little doubt, then, that Si and thus aerogel dominate most individual melt analyses in the tip, yet all show some Al contamination and a few are even dominated by Al.

The blunt face is covered by a mixture of particulate and fused material, with the latter being identifiable by rounded shapes and smooth surfaces of individual particles as seen in Fig. 14b and as detailed in Fig. 14h. All materials adhering to the blunt face typically contain only Si, with Al being exceptionally rare and, if present, in very low concentration. Most of the particulates covering the residue's flat face are thus aerogel, either molten or compressed, and on occasion sintered into aggregates.

Representative residues of the other experiments are shown in Fig. 15. The 60 μm/3.6 km s^{-1} residues (Figs. 15a and 15b) have modestly more aerogel adhering to their surfaces compared to those at 3.1 km s^{-1} (Fig. 13), yet their surfaces are pristine. In contrast, the 60 μm/5.2 km s^{-1} residues (Figs. 15c and 15d) are virtually indistinguishable from those at 6.1 km s^{-1}, save the occasionally more pronounced ridge of the latter. Residues from the high-velocity experiments with 35 μm and 100 μm projectiles are shown in Figs. 15e and 15f and 15g and 15h, respectively. The 35 μm impactors are qualitatively similar to the 60 μm residues, but Fig. 15e illustrates a specimen that seems to be exceptionally well endowed with melt. Somewhat surprisingly, the 100 μm impactors (Figs. 15g and 15h) suffered distinctly more mass loss than the smaller impactors at otherwise identical conditions. Figure 15 g seems more typical than 15h, the latter representing the extreme out of four recovered specimens. The parent track of the projectile shown in 15h did not differ from those of the others, however. Therefore, we can exclude some flawed impactor that might have been disrupted into a few large fragments or numerous smaller ones upon impact; such fragments would be manifested by parasitic tracks emanating from the main track. The absence of such fragment tracks suggests that the mass loss suffered by this specimen must have been gradual.

We do not have a good explanation for this apparent size-dependent mass loss as it seems contrary to viscous drag and associated ablation processes which decrease with increasing

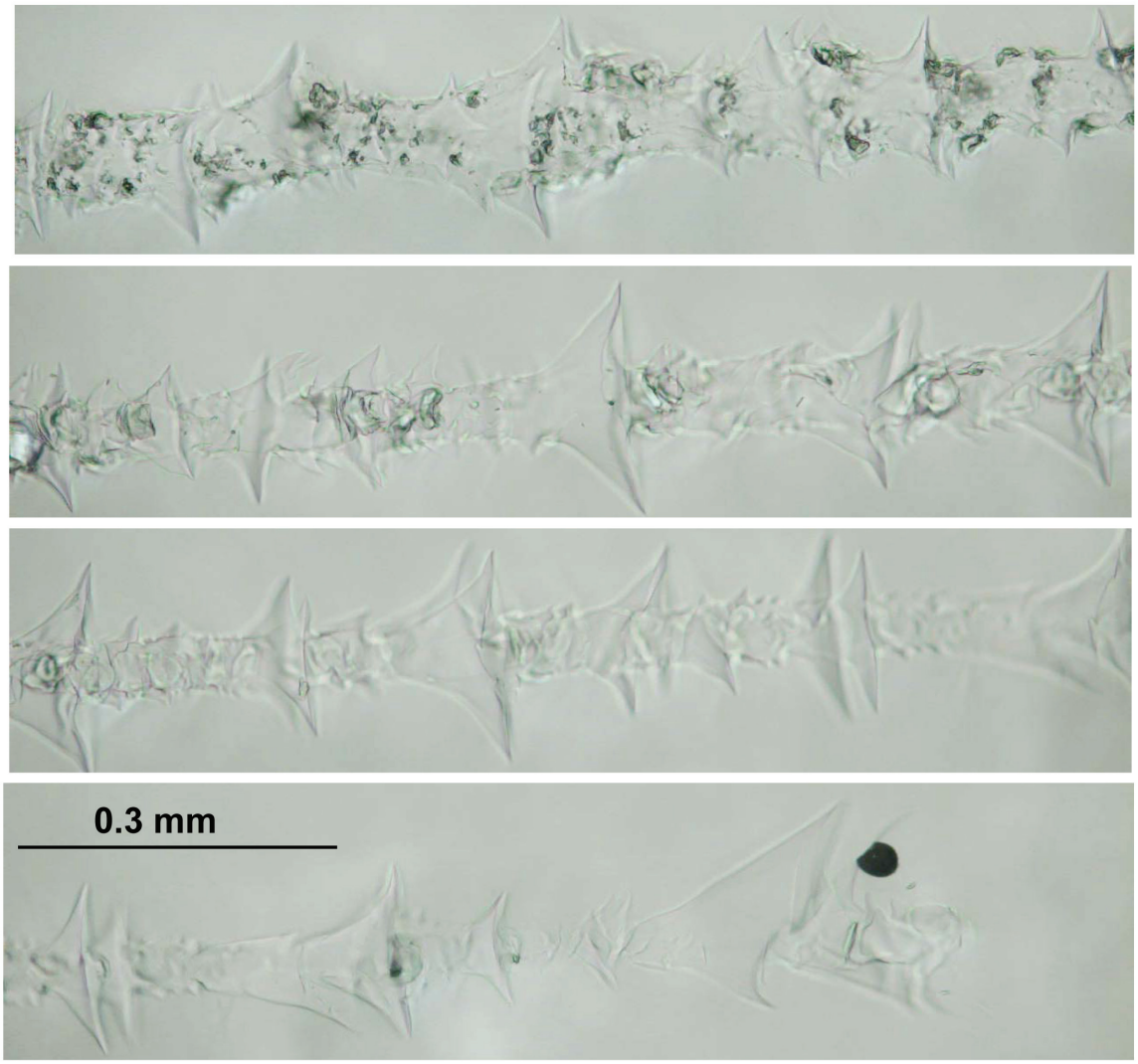

Fig. 11. Terminal portion of a single track from a 60 μm impactor at 6 km s^{-1}. Each panel is approximately 1 mm long, yet the panels are separated by gaps of ~2 mm along the axis of penetration. Note that the track becomes increasingly transparent with depth and the fracture systems develop progressively into complete cones, with large and small ones alternating in a highly regular, rhythmic fashion. Also note that the terminal projectile residue came to rest modestly off axis, a common occurrence.

particle size. It could relate to shock pulse duration, which increases with impactor size and that, in turn, would lead to a more prolonged thermal pulse, exposing the projectile to elevated temperatures for longer times. Also, the total kinetic energy per cross sectional area (ergs cm^{-2}) increases with size, specifically by a factor of almost 3 for spheres 35 and 100 μm in diameter.

Importantly, all of the projectiles recovered from the 3.1 and 3.6 kms^{-1} shots display pristine surfaces characterized by individual crystal faces of the polycrystalline precursors; none of the aerogel adhering to their surfaces is contaminated by Al. In contrast, all recovered projectiles at 5.2 km s^{-1} and higher speeds lack this polycrystalline surface texture and instead display smooth surfaces, as if molten. Invariably, the latter residues also develop a blunt face surrounded by a ridge, some melt patches on top of the smooth surfaces, and a conical melt tip antipodal to the blunt face. This melt tip invariably contains Al and thus consists of a mixture of molten aerogel and corundum. Al is exceptionally rare in the materials composing the ridge and adhering to the blunt face. The presence of Al containing melts at >5.2 km s^{-1} mandates temperatures > 2054 °C, the melting point of α-corundum.

The residues shown in Figs. 13–15 display distinctly bimodal modifications of the initially spherical impactor at the higher velocities: a blunt face contrasts with a nearly spherical segment that includes a melt tip. We suggest that the blunt face pointed forward and the spherical face rearward, with most melts flowing rearward and accumulating in the tip. Blunt, forward facing surfaces and rather intact, trailing surfaces are routinely observed for millimeter-sized metal projectiles impacting loose sand targets at <3 km s^{-1}.

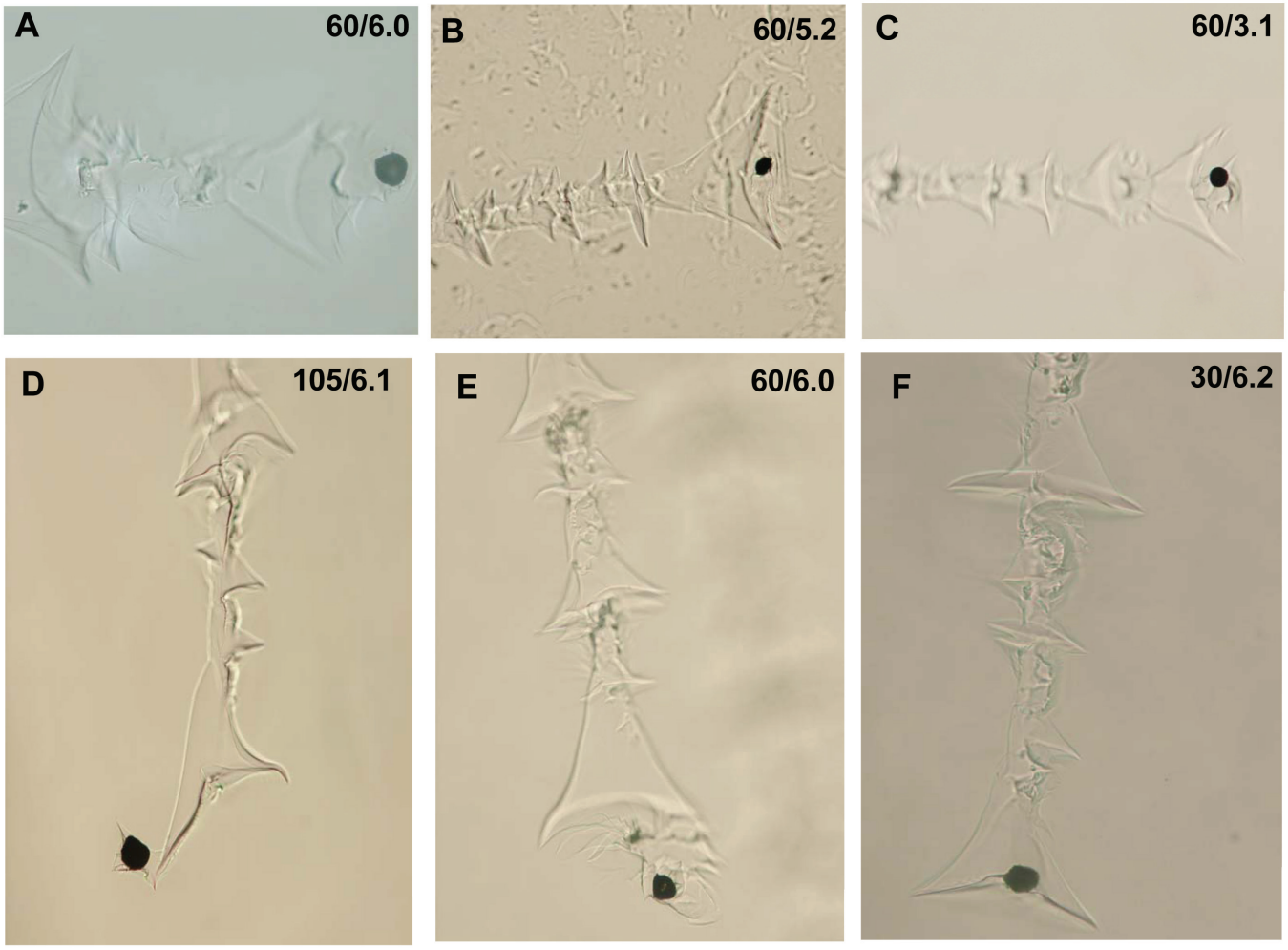

Fig. 12. Images of the termini and impactor residues for tracks produced by impactors of specific sizes and velocities (size/velocity in upper right hand corner). a–c) Experiments at identical size but variable V. d–f) Variable D_p and constant V. The images were taken at various magnifications with the nominal impactor sizes serving as internal scales.

Numerous sand fragments are embedded into the blunt surface, indicating that it was forward facing. Additionally, these large spheres are launched individually inside four-piece, serrated sabots that are spin stabilized by a rifled gun barrel. Without exception, the pristine, spherical face displays orthogonal burn marks that are caused by hot gunpowder gases leaking between the four orthogonal sabot segments. This "cross" of burn marks is thus a highly diagnostic marker of the projectile's rear. Also, stainless steel spheres can embed themselves deeply in soft Al 1100 targets; in situ observations reveal pristine, spherical rear surfaces and—after recovery—a forward pointing face that is blunt. Similar bimodal projectile shapes were also reported from penetrations into polymer foams by Tsou (1990). Finally, the blunt faces of the high-velocity residues are reminiscent of various reentry vehicles, suggesting that this is an aerodynamically stable shape and orientation. We are thus confident that the blunt face of our projectiles faced forward. It follows that materials adhering to the forward pointing face are substantially derived from the target and that materials shed from the penetrator will be deposited toward the rear.

Combining Figs. 13–15, a minimum of 5.2 km s^{-1} is needed to produce Al-contaminated melts. This implies that the melts could not have formed during stylus formation, as the latter is exclusively characterized by solid-state deformations. The melts must have formed in the main cavity, and been dragged to the terminus. Additionally, the preservation of these early and delicate melt features on the projectiles surface implies that there was no intimate contact between aerogel and the projectile's melt-covered surfaces for the entirety of stylus formation or >80% of the actual penetration. We suggest that the ridge of compressed aerogel effectively enlarges the projectile's diameter and appears to prevent some melts, formed in the cavity, from being stripped off the trailing edge. This ridge will thus play a critical role in decelerating the impactor and in preserving the rather delicate

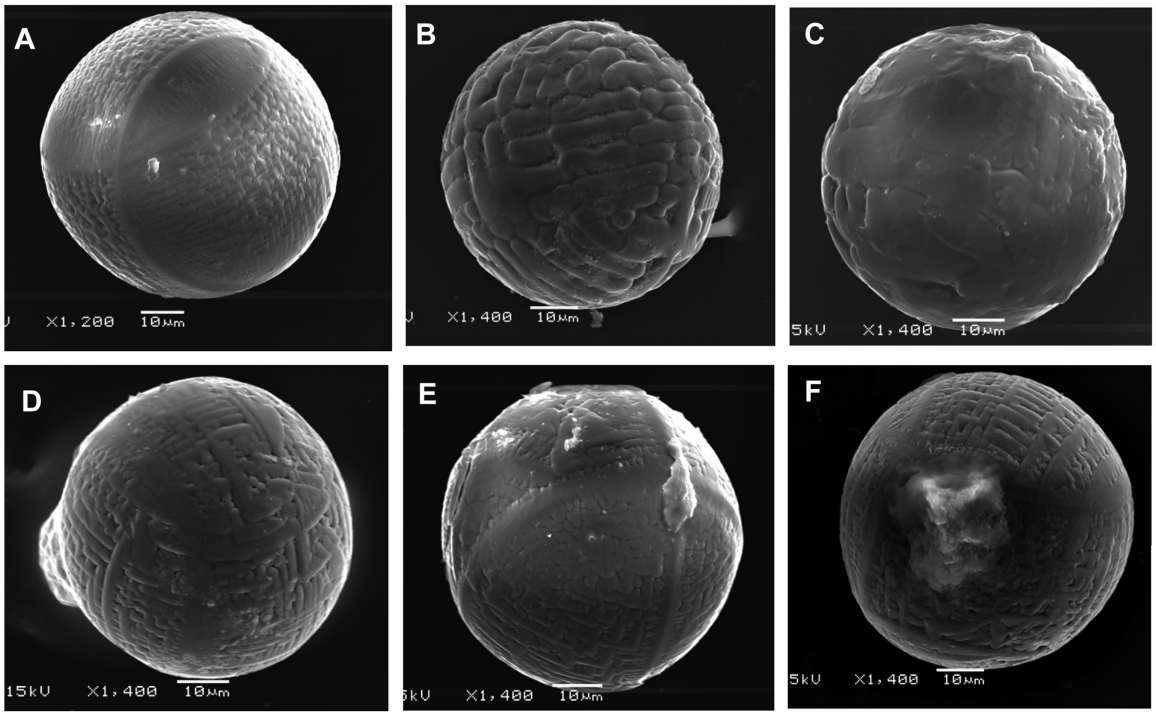

Fig. 13. Residues of 60 μm impactors recovered from the 3.11 km s^{-1} experiment. Note their polycrystalline surface textures akin to Fig. 1, suggesting that these low velocity impactors are substantially pristine.

melt features. Cumulatively, these observations also suggest that there can be very little tumbling of projectiles during penetration.

Summary of Track Morphology

Throughout these descriptions, we emphasized the high-velocity experiments, referring to their low-velocity counterparts only on occasion. This was deliberate, because the latter duplicate the deeper stylus sections of the high-velocity cases in all major morphologic aspects.

Formation of a main cavity seems intimately associated with melting phenomena. The latter include highly transparent, smooth walls as well as twisted, quasi-spiraling trails of clumped particulates that are intimately mixed with and bonded by aerogel melts. We also infer that all of the melts preserved on the surfaces of terminal particles were initially produced in the cavity. This includes melting of the refractory corundum at temperatures >2000 °C at 5.2 km s^{-1}. Some of these melts adhere to the projectiles' surfaces and end up at the track's terminus, because they are shielded from all of the ensuing penetration by a prominent ridge of compressed and partly molten aerogel. The absence of a major cavity at 3.6 km s^{-1} implies that only solid-state deformations occur at the more modest velocities, resulting in a long and slender stylus. The transition from main cavity to stylus is thus synonymous with the threshold velocity for melting of this particular aerogel, estimated to be at about 4 km s^{-1}. This then is also the likely exit velocity of the impactor emanating from the cavity in the high velocity cases.

Most of the penetration path, some 80% or more, is represented by the stylus and thus solid-state, mostly brittle, deformations. This stylus is dominated by spike like features and opaque particulates; the latter decrease in abundance with increasing depth. The terminal track sections are optically translucent and characterized by cone-in-cone features that differ distinctly from the spikes. The origin of either spikes or cone-in-cone structures is poorly understood, as is the systematic, regular spacing of large and small cones close to the terminus.

TRACK DIMENSIONS

Track dimensions were obtained through use of a compound microscope equipped with an automated X-Y table (Prior Optiscan with Image Pro read-out capabilities) that was calibrated with a micrometer scale. Precision of the measurements was ~2 μm and in many cases better than the observer's ability to precisely define a specific feature due to the somewhat fuzzy and blurred nature of typical track walls. Generally, some 10–20 individual tracks were surveyed per experiment. The averages of these measurements are tabulated in Table 1, including the definition of some parameters. Detailed measurements and their variations will be illustrated in the graphs to follow.

Total track length, for a constant 6 km s^{-1}, is illustrated in

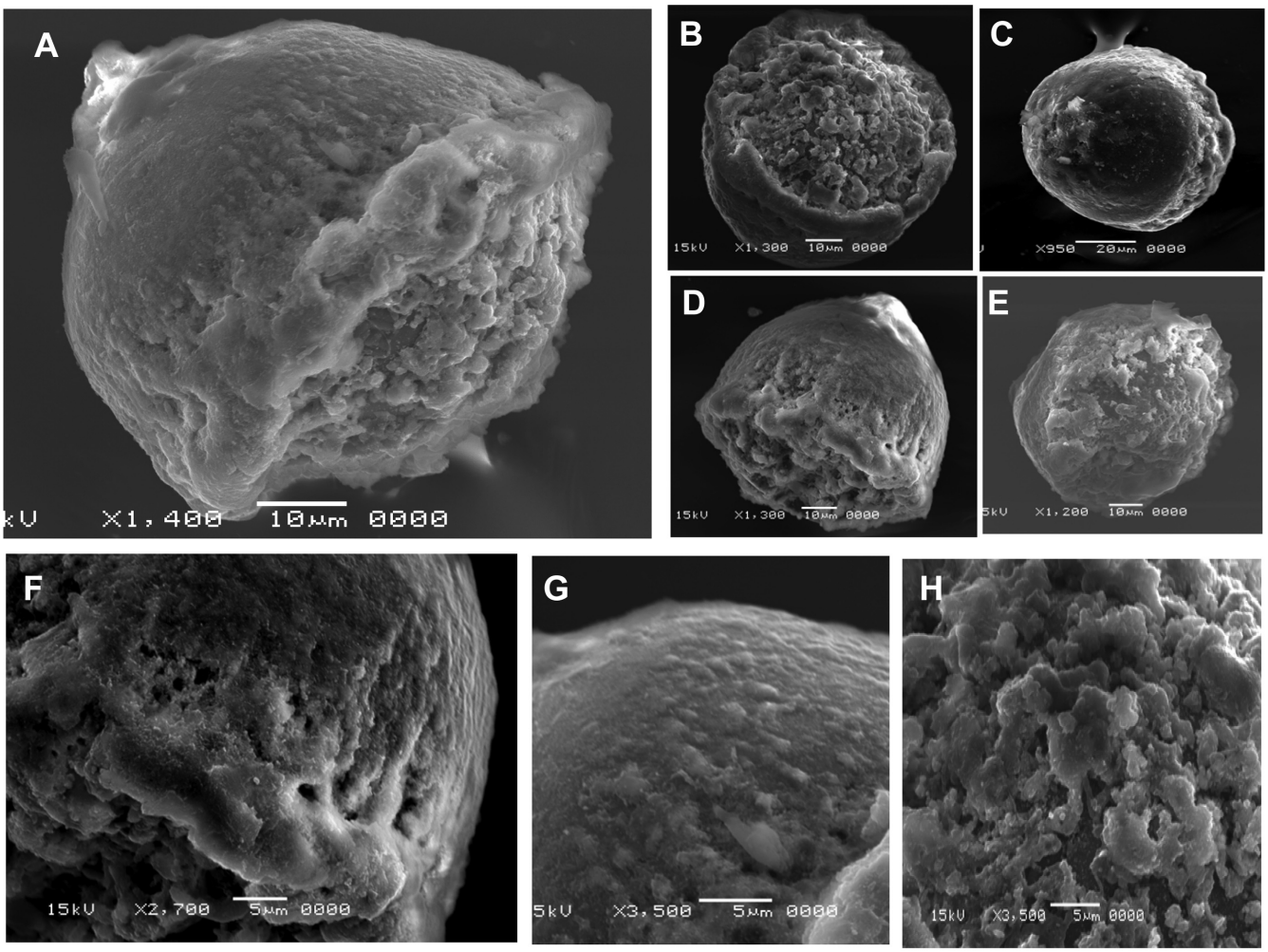

Fig. 14. Details of five individual residues (a–e) from the 60 µm/6 km s^{-1} experiment. All are characterized by a flat, forward-facing surface, a massive ridge of compressed and fused aerogel, and a distinct melt tip at the rear (when properly oriented). The bottom row (f–g) provides close-ups of melt stringers emanating from the aerogel ridge (f), a magnified view of melt splashes and droplets on the projectile's spherical surface (g), and details of the detroidal and molten materials adhering to the blunt faces (h). Figures (f) and (g) suggest melt flow towards the rear and eventual accumulation in a distinct tip. Also note there is no evidence for pristine, polycrystalline surfaces; all surfaces are smooth.

Fig. 16, with Fig. 16a showing the basic measurements for variable impactor sizes. The bin size is defined as $(L_{Tmax}-L_{Tmin})/10$ and varies with impactor size. The total track length scatters modestly, as expected from Fig. 2. Figure 16b plots the mean track length of Fig. 16a to summarize the general trends and for comparison with previous work, all at 6 km s^{-1}. A least-squares fit through the three new data points, forced to pass through the origin, has a slope of 0.60 (+0.02 std. err.). This compares with a much shallower slope and correspondingly much shorter tracks for the density-graded Stardust aerogel as found by Burchell et al. (2008), the only other study that systematically varied projectile size at speeds around 6 km s^{-1}. Also, single points at 6 km s^{-1} are illustrated in Fig. 16b, representing tracks from SLG spheres of comparable sizes, one launched into identical ODC (0.02 g cm^{-3}) aerogel (Hörz et al. 1998) and the other into somewhat denser (0.06 g cm^{-3}) targets (Burchell et al. (2001). All SLG impactors produced shorter tracks than their alumina counterparts, even those that encountered the top 10 mm of the Stardust collectors, nominally of 0.01 g cm^{-3} (Tsou et al. 2003) This is further illustrated via the "scaled" track depth in Fig. 16c, which normalizes the absolute track length to the respective impactor size(s). The only result with which the present experiments can be compared directly is the 50 µm SLG point of Hörz et al. (1998), as it employed the same ODC aerogel. The specific differences among the SLG experiments tend to scale qualitatively with aerogel density, considering that the single point from Burchell et al. (2001) refers to 0.06 g cm^{-3} targets.

In summary, we observe that corundum projectiles penetrate approximately a factor of 2.5 deeper than SLG impactors at 6 km s^{-1}. The densities of corundum and SLG account for some of this difference in track lengths, yet other rheological properties of the projectiles may also play a role,

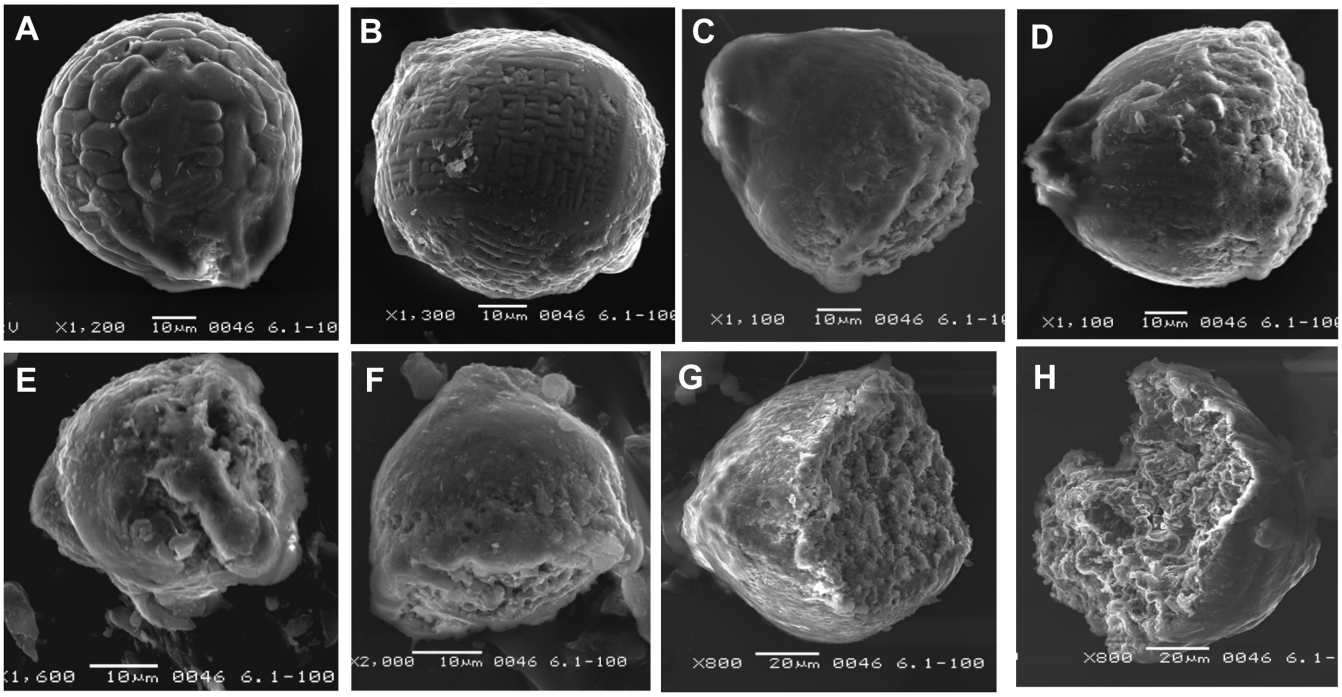

Fig. 15. Representative residues of 60 µm impactors from the 3.6 km s^{-1} (A, B), and the 5.2 km s^{-1} (C, D) experiments. Also shown are the residues of 35 µm projectiles at 6.2 km s^{-1} (E, F), and of the 105 µm impactors at 6.1 km s^{-1} (G, H). Please consult the text for details.

Table 1. Summary of track dimensions obtained by spherical corundum projectiles into SiO_2-based aerogel of density 0.02 g cm^{-3}. All length (L) measurements are from the original target surface.

Projectile diameter (D_P, mm)	Impact velocity (V, km s^{-1})	Track length, total (L_T, mm)	Maximum track width (D_{Tmax}, mm)	Depth to start of D_{Tmax} (L_1, mm)	Depth to end of D_{Tmax} (L_2, mm)	Track volume (V_T, mm^3)	Diameter of residue (D_R, µm)
35	6.18	17.52	0.395	0.91	1.70	2.27	35.2
60	6.04	34.57	1.042	2.14	4.81	9.95	63.2
105	6.10	61.05	1.350	3.48	9.65	39.01	112.1
60	5.21	37.67	0.702	1.51	3.40	5.77	59.8
60	3.64	36.63	0.423	1.29	2.61	3.58	62.3
60	3.11	37.67	0.425	n.a.	n.a.	1.49	62.7

such as mechanical strength and melting point. Specifically, Trucano and Grady (1995) suggest that strength properties are important as they control the deformation of the impactor upon contact and its ensuing fragmentation, all of which affect total penetration depth.

We now address the velocity-dependent penetration effects for Al_2O_3 impactors of constant size (60 µm) as illustrated in Fig. 17. Surprisingly, most tracks are comparable in length over a velocity range from 3 to 6 km s^{-1} (Fig. 17a). The present trends are consistent with the earlier work of Hörz et al. (1998, ODC aerogel) and Burchell et al. (2001, 0.06 g cm^{-3}; D_P = 106 µm), as illustrated in Fig. 17b. All three studies varied velocity systematically and suggest that track length goes through a modest maximum (L_{Tmax}) at some specific velocity. Burchell et al. (2001; see their Fig. 4) experimented systematically with aerogels of still higher densities and demonstrated that L_{Tmax} strongly depends on aerogel density, with the penetration maximum shifting to lower velocities with increasing aerogel density. This is consistent with Trucano and Grady (1995), as higher target densities should promote increased deformation and flattening of the SLG impactors; also, higher impact speeds should promote ablation and thus loss of mass from the penetrating object. L_{Tmax} for the present alumina shots occurs near 5 km s^{-1} and is thus modestly higher than for SLG shots into identical aerogel. Lastly, Fig. 17c presents the scaled track lengths and accounts best for the relatively large SLG impactors used by Burchell et al. It appears that the projectiles of Burchell et al. deformed most because they encountered the densest target(s). The difference between the present work and the SLG shots of Hörz et al. into the same aerogel relates to projectile properties only and suggests that the corundum projectiles deform and ablate less than SLG impactors. The Al_2O_3 spheres are, therefore, the superior penetrators.

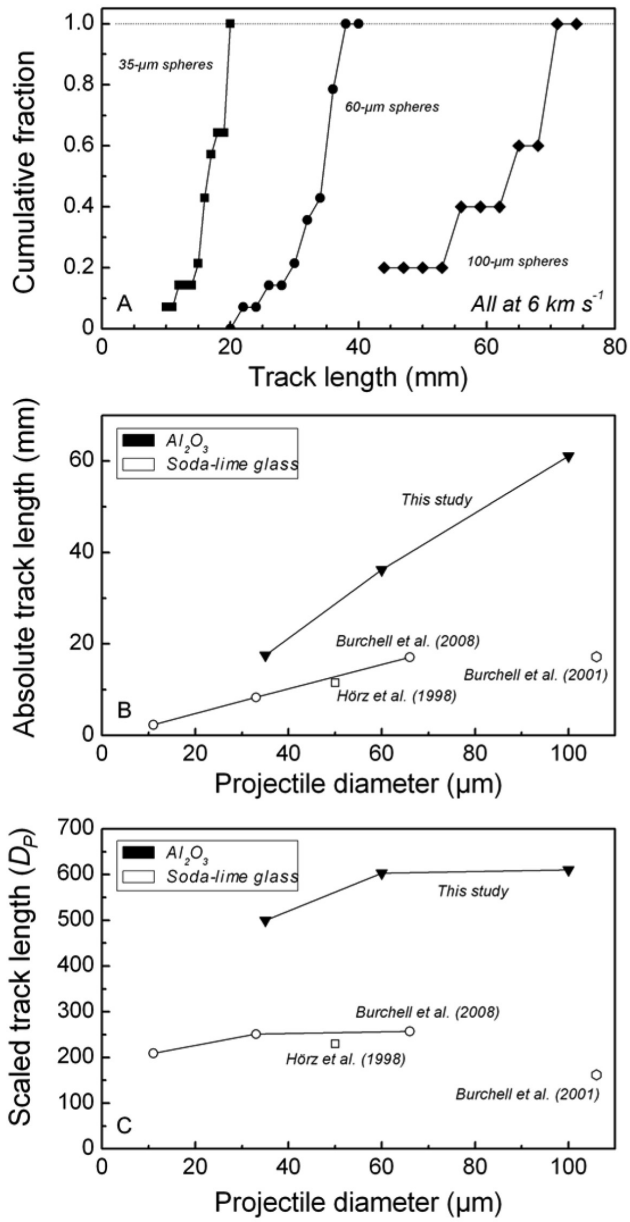

Fig. 16. Measured track lengths and comparison with those from other aerogel experiments employing SLG projectiles of variable D_P at constant impact velocity (~6 km s^{-1}). A) Cumulative distribution of absolute track lengths in present study. B) Comparison of average track length resulting from Al_2O_3 and soda-lime glass (SLG) projectiles. C) Track length normalized to projectile dimensions for Al_2O_3 and SLG projectiles; note that the corundum impactors penetrate approximately a factor of 2.5 deeper than SLG projectiles.

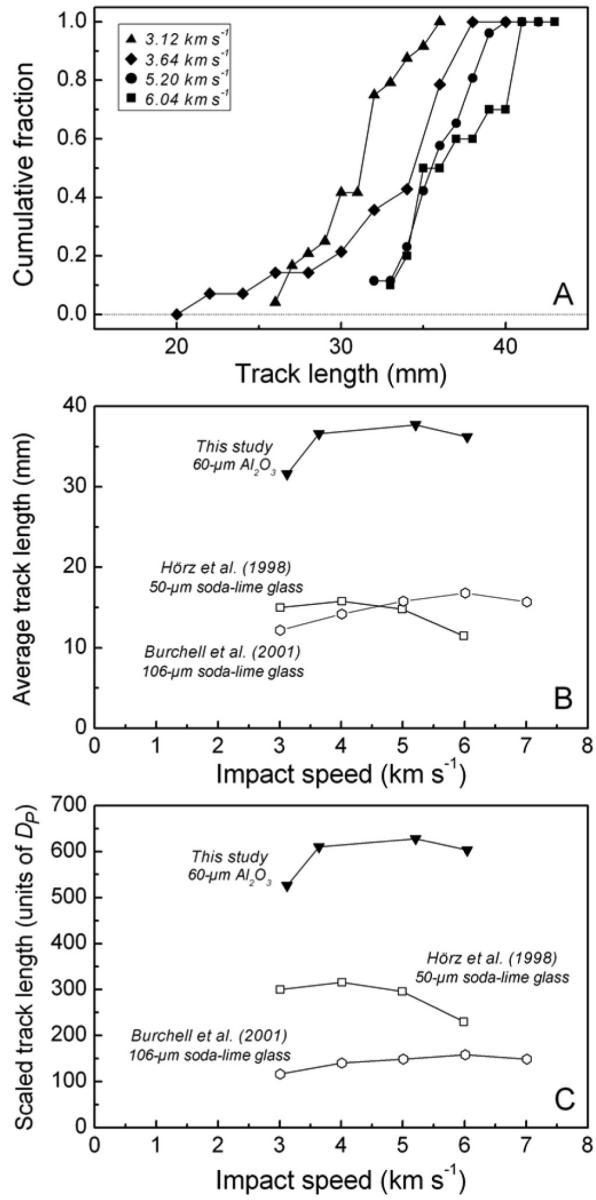

Fig. 17. Measurements of track length and comparison with other experiments for impactors of constant D_P and variable velocity. A) Cumulative distribution of track lengths as a function of impact speed for 60 μm Al_2O_3 projectiles; note that the mean track lengths vary only modestly with velocity. B) Comparison of average track length for Al_2O_3 impactors with other experimental studies using SLG projectiles. C) Track length normalized to projectile dimensions for the present and earlier experiments. Note that surprisingly modest velocity dependence is observed in all of these systematic studies.

The observations depicted in Figs. 16 and 17 appear to be internally inconsistent if viewed from a kinetic energy point of view, with the experiments at variable impactor mass being strongly dependent on kinetic energy, yet those at constant projectile mass and variable velocity only modestly so. This is entirely due to the fact that the stylus feature totally dominates absolute track length for the limited range of experimental impact speeds. Most of the velocity-dependent phenomena manifest themselves in the main cavity which is only some 10–20% of the total penetration depth.

To demonstrate this, we measured the maximum track width (D_{Tmax}) and plot it in Fig. 18a for the variable size/constant velocity tests and in Fig. 18b for the variable velocity/constant size experiments. Accordingly, track

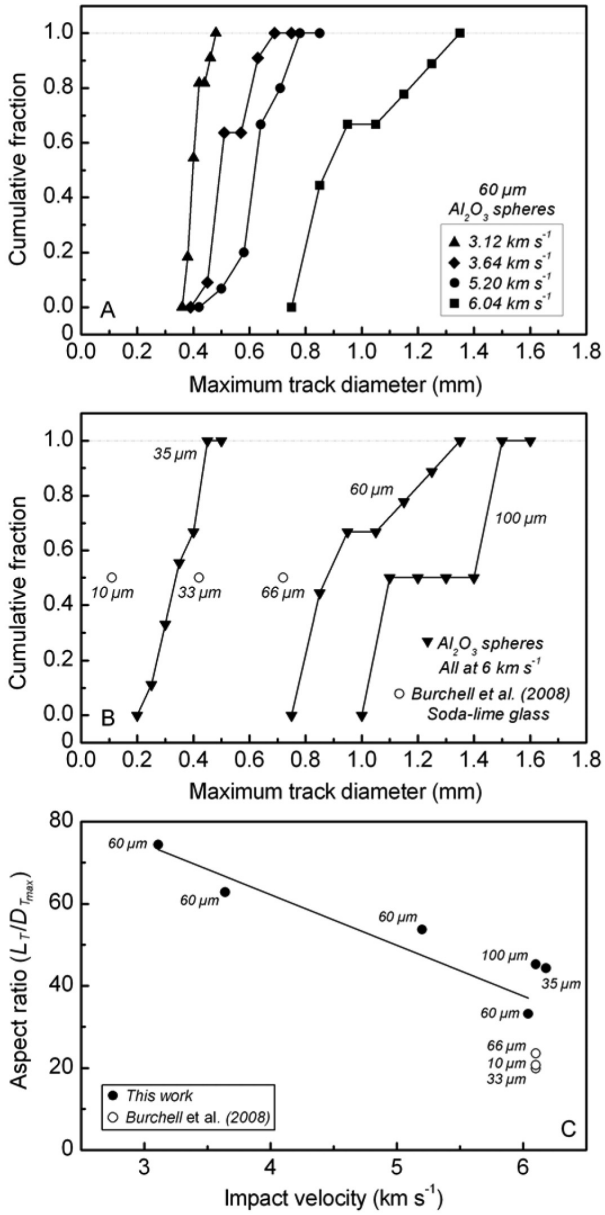

Fig. 18. Measurements of maximum track diameter and comparison with the Stardust calibrations of Burchell et al. (2008) using soda lime glass; the variables are defined in Table 1. A) Cumulative distribution of track widths from Al_2O_3 experiments at constant V and variable D_p; note that D_{Tmax} increases systematically with V. B) Cumulative distribution of D_{Tmax} for Al_2O_3 experiments at constant V and variable D_P. Also, the average D_{Tmax} data of Burchell et al. are plotted on the "mean" (50%) horizontal line and located at their corresponding D_P. Note that the datum of Burchell et al. for 33 µm projectiles is modestly larger than that of our 35 µm case, but their 66 µm datum appears to be smaller than our 60 µm case. C) Comparison of the aspect ratios (L_T/D_{Tmax}) of aerogel tracks as a function of velocity. Note the systematic behavior of the constant D_P and variable V experiments of the present study. The data points at constant V and variable D_P scatter somewhat, yet they are readily distinguishable as a group from the 5.2 km s^{-1} experiments as well as from the SLG shots into Stardust aerogel, the latter resulting in distinctly stubbier tracks than those from the corundum impacts.

diameter increases with both size and velocity. Figure 18c illuminates the scaled dimensions of both experimental series and plots the tracks' aspect ratios (L_T/D_{Tmax}) against velocity. There is a strong dependence of this aspect ratio on velocity, as the low-velocity tracks are systematically more slender than those at higher velocities, because the latter develop main cavities with increasingly larger diameters. The experiments at constant 6 km s^{-1} and variable impactor size scatter somewhat, yet all tracks are wider than those from the 5.2 km s^{-1} experiment. Other than the Stardust aerogel experiments of Burchell et al. (2008), there are no additional D_{Tmax} measurements detailed in the experimental literature. These Stardust simulations produced roughly comparable cavity diameters at ~6 km s^{-1} as illustrated by the average diameters of Burchell et al. (2008) which are plotted on the 50% mean diameter line in Fig. 18b. The Stardust SLG shots scatter from D_{Tmax} = 10.9 − 12.7 D_P, while the Al_2O_3 tracks range from D_{Tmax} = 11.28 − 17.37 D_P, suggesting modestly larger cavities for corundum. The aspect ratios in Fig. 18c differ systematically as a function of velocity and demonstrate that it is predominantly total penetration depth that differs among these data sets, rather than cavity diameter. By comparison, all SLG tracks are relatively stubby, as they are so much shorter than the Al_2O_3 tracks, yet their cavity diameters approach those of the corundum tracks. This identifies the latter as unusually slender features.

Having introduced track lengths and maximum diameters, we now address track volume and total mass displaced. Burchell et al. (2001, 2008) modeled their tracks as two truncated cones (e.g., Fig. 1 in Burchell et al. 2008). We adopted this approach, but we separated the cones by a cylindrical volume of diameter D_{Tmax} and length $L' = L_2 - L_1$. This geometry was judged to represent our unusually deep tracks more adequately, especially their main cavities, which displayed relatively constant widths and cylindrical shapes bounded by depths L_1 and L_2 (see Fig. 4). These volume calculations are summarized in Fig. 19 and plotted against kinetic energy. The results at constant 6 km s^{-1} and variable impactor size define a least-squares fit that has a slope of 0.87 (+0.25 std. err.). This differs distinctly from the slope of the constant mass/variable velocity tracks of 1.27 (+0.04 std. err.), which is greatly driven by the 3.1 km s^{-1} experiment at the lowest kinetic energy. Obviously, the latter lacks a main cavity and the relatively small volume is real. It is the 60 µm/3.6 km s^{-1} experiment that seems to be the (modest) outlier in this trend, judging from the 5.2 km s^{-1} datum with a main cavity that is, as expected, smaller than that of the 6 km s^{-1} case. These distinctly different slopes suggest that velocity-dependent effects on cavity volume, such as the presence or absence of a main cavity and its overall length (see Table1) are more dominant than are projectile size-dependent effects, which produce volumes that scale approximately linearly with D_P, as their slope is close to 1 at constant encounter velocity.

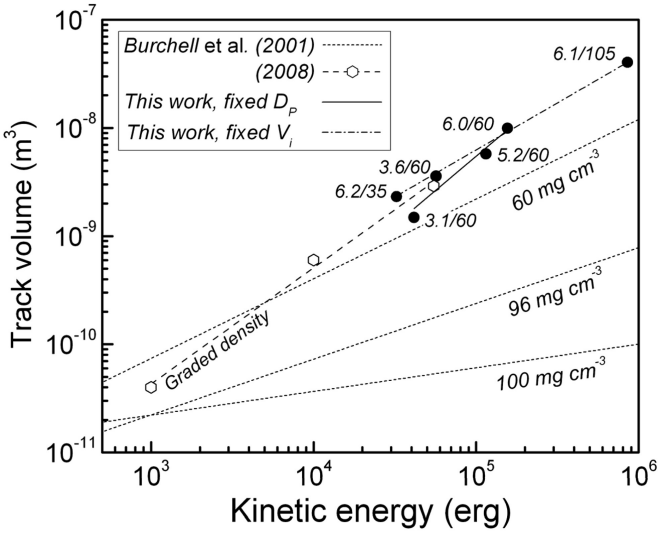

Fig. 19. Kinetic energy versus absolute track volume for the present Al_2O_3 experiments into 0.02 g cm^{-3} aerogel and comparison with those of SLG impacts into density gradient Stardust aerogel (Burchell et al. 2008); also shown are data from Burchell et al. (2001) who fired SLG into aerogel targets of variable, relatively high densities. See text for detailed discussion.

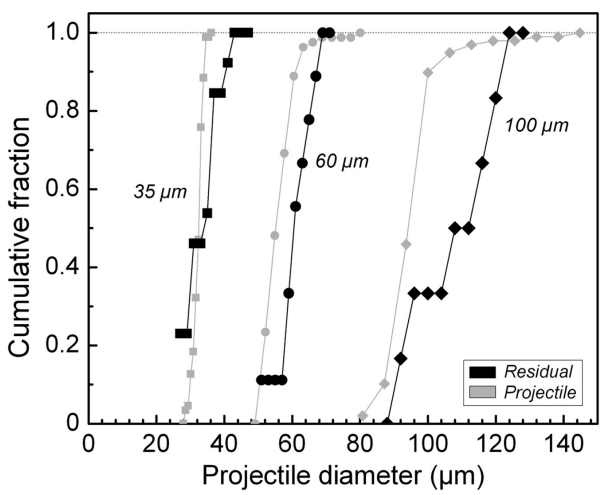

Fig. 20. Measurements of the residue diameters observed in situ via a compound microscope for the 6 km s^{-1} experiments. The diameters of the residues are apparently increased over those of the initial impactors by the accumulation of dense, optically opaque aerogel that could not be discerned from the Al_2O_3 core in transmitted light.

The Stardust calibrations of Burchell et al. (2008) produced tracks at constant velocity and variable mass, as did our size-dependent experiments. Indeed, they obtain a slope that is nearly identical to that describing the equivalent Al_2O_3 data, thus corroborating an approximately linear relationship between displaced aerogel mass and impactor mass at constant velocity. Even absolute track volumes are surprisingly similar in these two studies. In detail, the Stardust SLG tracks are, however, modestly less voluminous than the Al_2O_3 tracks at similar energies, because the main cavities of SLG impactors are smaller than those of the Al_2O_3 projectiles. Considering the vastly different targets and projectiles between the present work and the Stardust calibrations, we judge the close agreement in absolute track volume entirely fortuitous. It might even be incorrect to plot the density-graded aerogel data in Fig. 19, because each projectile size class of Burchell et al. (2008) encountered and penetrated targets of different bulk density at depth.

The Burchell et al. (2001) study launched impactors of constant size (105 μm, SLG) at different velocities into aerogels of different densities. Their results are thus equivalent to our variable velocity experiments represented by the steeper slope. As pointed out by Burchell et al. (2001), the track volume critically depends on aerogel density, with the relative efficiency of aerogel displacement (the slope) becoming progressively larger (steeper) with decreasing target density. Our experiments, yielding the steepest slope, nicely complement and extend the trend of Burchell et al. to target densities of 0.02 g cm^{-3}.

As illustrated in Fig. 11, the impactor residues are readily observed and their sizes measured under the optical microscope. Figure 20 presents the average diameters, typically some 10–20 residues per experiment, and the averaged value of some 2–4 measurements per residue, for the 6 km s^{-1} shots. Very interestingly, these residue measurements produced sizes modestly larger than those of the initial impactors. We double-checked and eliminated systematic calibration errors of the optical microscope and SEM, the latter being used for the pre-shot population. The optical, in situ measurements reflect our inability to distinguish between the real Al_2O_3 core and the adhering aerogel, as we measure the silhouette of an essentially opaque object. Care is thus necessary to infer projectile sizes from optical in situ measurements.

DISCUSSION

We have already offered inferences and interpretations throughout the morphologic description of our tracks, and we placed their absolute dimensions into the existing context of other laboratory experiments. We ascribe the modestly more bulbous cavities and shorter styli reported from SLG experiments to the incipient deformation, primarily by flattening, of glass projectiles upon impact; corundum deforms less and is therefore the superior penetrator, producing exceptionally slender tracks. These considerations naturally extend to the formation of some exceptionally bulbous cavities observed on Stardust (Brownlee et al. 2006), which demand even more projectile deformation, if not complete disruption and mechanical dispersion of individual fragments (Hörz et al. 2006; Burchell et al. 2008; Trigo-Rodríguez et al. 2008).

Below we focus on the thermal environment during

aerogel impacts. Our projectiles recovered from the 5.2 km s^{-1} experiment revealed melting of corundum and thus temperatures >2050 °C. We attempted to identify Al-bearing materials in the interior walls of bisected tracks via SEM-EDS methods. However, these attempts failed because Al is below the detection threshold at modest cumulative counts and gets swamped by the neighboring Si and aerogel contaminants (Na) as higher counts accumulate. We thus do not know currently where the material lost from the projectile resides along the track.

Pervasive melting and mixing of projectile material with aerogel melts is observed on Stardust (e.g., Brownlee et al. 2006; Zolensky et al. 2006; Keller and Messenger 2008). It was also found in 0.03 g cm^{-3} aerogel by Noguchi et al. (2007) who used serpentine and cronstedtite projectiles at speeds as low as 4 km s^{-1}; these minerals have decomposition temperatures of 470 °C (Caillere and Henin 1957) and 500–600 ºC (depending on specific composition; Nozaki et al. 2006), respectively. Noguchi et al. (2007) also launched well-sieved fragments of Murchison meteorite that revealed melting of serpentine and cronstedtite, but not of pyroxene (diopside) under comparable conditions, limiting T to <1390 °C. They estimate the prevalent temperatures based on mineralogical criteria of the recovered impactors to be as high as 1400 °C. Interestingly, significantly higher temperatures, some 2000 °C, were inferred from the spectral analysis of the impact light flash generated during these experiments (Noguchi et al. 2007), yet this temperature may refer to the shocked target only and not necessarily to the impactor.

Additionally, Ishii et al. (2008a) reported on experiments in which powdered pyrrhotite (FeS) impacted Stardust aerogel at 6 km s^{-1}. These experiments not only produced mixed melts of projectile and target materials along the track walls, but they also demonstrated reduction of FeS to metallic Fe, as manifested by submicron-sized particles of pure Fe disseminated throughout the glassy matrix. A follow-up study (Ishii et al. 2008b) determined that the volatile S decoupled from the Fe and diffused into the surrounding aerogel over distances an order of magnitude larger than the Fe. Although poorly defined, these processes mandate elevated temperatures, with at a minimum of 1000 K (Ishii et al. 2008a).

It is important to note that the peak pressures upon 6 km s^{-1} impacts with typical aerogel (<5 GPa; Dominguez et al. 2004; Anderson and Cherne 2008) are nowhere close to the pressures needed to melt natural minerals composing cometary dust (>40 GPa; e.g., Stöffler 1972). Consistent with these modest stresses and associated temperatures, the interiors of many residues recovered from Stardust are modestly shocked, if shocked at all. As a consequence, the thermal environment during aerogel penetration seems entirely dictated by the highly porous aerogel itself, the major thesis of Anderson and Cherne (2008), who postulate aerogel temperatures as high as 8,000 K for typical impacts at 6 km s^{-1}. Natural silicates in contact with this extremely hot aerogel begin to decompose or melt straightforwardly (depending on mineral species), to form melt mixtures of aerogel and projectile species. This then identifies the projectile-containing melts in the walls of aerogel tracks as a mixture of shock-molten aerogel that was contaminated by thermally induced decomposition or melting of projectile minerals. We consider this distinction of melt derivation significant as it may lead to mineral-specific fractionation effects at specific temperatures, as well as to "whole rock" melts if the thermal environment were sufficiently severe to melt all component minerals. Obviously, this radiative thermal processing and melting occurs predominantly at the projectile's surfaces and may be viewed as an extreme form of "flash heating." As attested to by Stardust observations, this thermal processing can be very selective, affecting fine-grained projectile components much more so than coarse particles (Brownlee et al. 2006). Although the resulting melts might be indistinguishable from genuine ablation products, as both derive from the particle's surfaces, we suggest that ablation may play a minor role. The dominant thermal effects seem to arise from intimate contact with extremely hot aerogel, representing some extreme form of flash heating.

CONCLUSIONS

We employed corundum projectiles to complement other systematic studies, based on glass impactors, into the penetration behavior of SiO_2-based aerogel. As expected, the highly refractory and mechanically strong Al_2O_3 is the superior penetrator, making tracks approximately 2.5 times as deep as soda-lime glass projectiles of the same size. When measured in isolation, none of the dimensional parameters, such as track length, track width, entrance hole diameter, or cavity length are very reliable criteria for estimating initial impactor size. This is in contrast to total displaced volume which scales systematically with E_{kin}. This conclusion is not new, however, having been reached earlier by Burchell et al. (2001, 2008).

The exceptionally deep and slender tracks produced by the corundum impactors are entirely dominated by the anomalously long stylus portion, which represents solid-state processes at velocities <4 km s^{-1}. A sizable cavity close to the target surface is produced only at higher speeds and mandates melting of the aerogel target; it even includes melting of the corundum projectiles at speeds >5.2 km s^{-1}, implying temperatures >2000 °C. The latter refers to the melting of the projectile surfaces in contact with aerogel, the temperature of which may very well be significantly higher (>5000 °C) based on Anderson and Cherne (2008). The thermal environment during aerogel capture on dedicated sample return missions can thus be extreme, as manifested by detailed TEM studies of the track walls and terminal particles from Stardust (e.g., Brownlee et al. 2006; Zolensky et al.

2006; Keller and Messenger 2008), and through examination of experimental tracks (Noguchi et al. 2007; Ishii et al. (2008a, 2008b). This melting, however, takes place at the projectiles' surfaces and the interiors of many residues might actually be rather pristine. Indeed, many Stardust particles are thought to be aggregates composed of a fine-grained matrix and relatively large clasts; it is this matrix that melts preferentially, because it disperses with ease into its fine-grained components that will be exposed to the hot aerogel; the larger clasts suffer surface melting only and may survive capture with their interiors relatively intact.

Our SEM-EDS analyses of recovered projectile residues reveal ample evidence for melts that originally formed in the main cavity and were dragged over considerable distances to the track's terminus. This mandates that there was no contact of the trailing surfaces with aerogel for some 80% of the total penetration path, because a substantial, circumferential ridge effectively enlarges the projectile diameter; the latter must thus be present when the penetrator exits the main cavity. Projectiles recovered from >5.2 km s^{-1} typically exhibit blunt forward-pointing faces and relatively spherical surfaces on the trailing edge, suggesting that the impactors do not rotate for most of the penetration. The massive, circumferential ridge separates these two surfaces and seems to play a critical role; such ridges are not part of any current model addressing the high-speed penetration of highly porous, low-density media.

While the separation of shock effects from those induced by viscous drag during the penetration of highly porous, low-density media (Anderson and Ahrens 1994) is conceptually appealing, the present study and the analysis of Stardust samples suggest that most projectile melting may not be accomplished by ablation, but by exposure to aerogel that was shocked to extreme temperatures. This flash heating affects only the surfaces of large grains, but it may totally consume highly dispersed, fine-grained materials. Future aerogel impact experiments and thermodynamic considerations, possibly including experiments with short-pulsed lasers, will therefore be needed to understand these thermal effects at time scales of nano- to microseconds.

Editorial Handling—Dr. Donald Brownlee

REFERENCES

Ahrens T. J. and Cole D. M. 1974. Shock compression and adiabatic release of lunar fines from Apollo 17. Proceedings, 5th Lunar and Planetary Science Conference. pp. 2333–2345.

Anderson W. W. and Ahrens T. J. 1994. Physics of interplanetary dust capture via impact into organic polymer foams. *Journal of Geophysical Research* 99:2063–2071.

Anderson W. W. and Cherne F. J. 2008. Model development for assessment of thermal histories of returned Stardust cometary dust samples. 39th Lunar and Planetary Science Conference. Abstract #2540.

Barrett R. A., Zolensky M. E., Hörz F., Lindstrom D. J., and Gibson E. K. 1992. Suitability of silica aerogel as a capture medium for interplanetary dust. Proceedings, 22nd Lunar and Planetary Science Conference. pp. 203–212.

Brownlee D., Tsou P., Aléon J., Alexander C. M. O'D., Araki T., Bajt S., Baratta G. A., Bastien R., Bland P., Bleuet P., Borg J., Bradley J. P., Brearley A., Brenker F., Brennan S., Bridges J. C., Browning N., Brucato J. R., Brucato H., Bullock E., Burchell M. J., Busemann H., Butterworth A., Chaussidon M., Cheuvront A., Chi M., Cintala M. J., Clark B. C., Clemett S. J., Cody G., Colangeli L., Cooper G., Cordier P. G., Daghlian C., Dai Z., D'Hendecourt L., Djouadi Z., Dominguez G., Duxbury T., Dworkin J. P., Ebel D., Economou T. E., Fairey S. A. J., Fallon S., Ferrini G., Ferroir T. Fleckenstein H., Floss C., Flynn G., Franchi I. A., Fries M., Gainsforth Z., Gallien J.-P., Genge M., Gilles M. K., Gillet P., Gilmour J., Glavin D. P., Gounelle M., Grady M. M., Graham G. A., Grant P. G., Green S. F., Grossemy F., Grossman L., Grossman J., Guan Y., Hagiya K., Harvey R., Heck P., Herzog G. F., Hoppe P., Hörz F., Huth J., Hutcheon I. D., Ishii H., Ito M., Jacob D., Jacobsen C., Jacobsen S., Joswiak D., Kearsley A. T., Keller L., Khodja H., Kilcoyne A. L. D., Kissel J., Krot A., Langenhorst F., Lanzirotti A., Le L., Leshin L., Leitner J., Lemelle L., Leroux H., Liu M.-C., Luening K., Lyon I., MacPherson G., Marcus M. A., Marhas K., Matrajt G., Meibom A., Mennella V., Messenger K., Mikouchi T., Mostefaoui S., Nakamura T., Nakano T., Newville M., Nittler L. R., Ohnishi I., Ohsumi K., Okudaira K., Papanastassiou D. A., Palma R., Palumbo M. O., Pepin R. E., Perkins D., Perronnet M., Pianetta P., Rao W., Rietmeijer F., Robert F., Rost D., Rotundi A., Ryan R., Sandford S. A., Schwandt C. S., See T. H., Schlutter D., Sheffield-Parker J. A., Simionovici S., Sitnitsky S. I., Snead C. J., Spencer M. K., Stadermann F. J., Steele A., Stephan T., Stroud R., Susini J.,. Sutton S. R., Taheri M., Taylor S., Teslich N., Tomeoka K., Tomioka N., Toppani A., Trigo-Rodríguez J. M., Troadec D., Tsuchiyama A., Tuzolino A. J., Tyliszczak T., Uesugi K., Velbel M., Vellenga J., Vicenzi E., Vincze L., Warren J., Weber I., Weisberg M., Westphal A. J., Wirick S., Wooden D., Wopenka B., Wozniakiewicz P. A., Wright I., Yabuta H., Yano H., Young E. D., Zare R. N., Zega T., Ziegler K., Zimmerman L., Zinner E., and Zolensky M. 2006. Comet Wild 2 under a microscope. *Science* 314:1711–1716.

Burchell M. J., Creighton J. A., Cole M. J., Mann J., and Kearsley A. T. 2001. Capture of particles in hypervelocity impacts in aerogel. *Meteoritics & Planetary Science* 36:209–221.

Burchell M. J., Graham G., and Kearsley A. 2006. Cosmic dust collection in aerogel. *Annual Review of Earth and Planetary Science* 34:385–418.

Burchell M. J., Fairey S. A. J., Wozniakiewicz P., Brownlee D. E., Hörz F., Kearsley A. T., See T., Tsou P., Warren J., Westphal A., Green S. F., Trigo-Rodríguez J. M., and Domínguez G. 2008. Characteristics of cometary dust tracks in Stardust aerogel and laboratory calibrations. *Meteoritics & Planetary Science* 43: 23–40.

Calliere S. and Henin S. 1957. The chlorite and serpentine minerals, In *The differential thermal investigation of clays*, edited by McKenzie R. C. London: UK Mineralogical Society. pp. 207–230.

Domínguez G., Westphal A. J., Jones S. M., and Phillips M. L. F. 2004. Energy loss and impact cratering in aerogels: Theory and experiment. *Icarus* 172:613–624.

Gratz A. J., Nellis W. J., and Hinsey N. A. 1993. Observations of high-velocity, weakly shocked ejecta from experimental impacts. *Nature* 363:522–524.

Hörz F., Cintala M. J., Zolensky M. E., Bernhard R. P., Davidson W. E., Haynes G., See T. H., Tsou P., and Brownlee D. E. 1998. Capture of hypervelocity particles with low density aerogel. NASA TM-98–201792. 58 p.

Hörz F., Zolensky M. E., Bernhard R. P., See T. H., and Warren J. L. 2000. Impact features and projectile residues in aerogel exposed on Mir. *Icarus* 147:559–579.

Hörz F., Bastien R., Borg J., Bradley J. P., Bridges J. C., Brownlee D. E., Burchell M. J., Cintala M. J, Dai Z. R., Djouadi Z., Dominguez G., Economou T. E., Fairey S. A. J., Floss C., Franchi I. A., Graham G. A., Green S. F., Heck H., Hoppe P., Huth J., Ishii H., Kearsley A. T., Kissel J., Leitner J., Leroux H., Marhas M., Messenger K., Schwandt C. S., See T. H., Snead S., Stadermann F. J., Stephan T., Stroud R., Teslich N., Trigo-Rodríguez J. M., Tuzzolino A. J., Troadec D., Tsou P., Warren J., Westphal A., Wozniakiewicz P. J., Wright I., and Zinner E. 2006. Impact features on Stardust and comet Wild 2 dust. *Science* 314:1716–1719.

Ishii H. A., Bradley J. P., Dai Z. R., Chi M., Kearsley A. T., Burchell M. J., Browning N. D., and Molster F. 2008a. Comparison of comet 81P/Wild 2 dust with interplanetary dust from comets, *Science* 319:447–450.

Ishii H. A., Brennan S., Bradley J. P., Pianetta P., Kearsley A. T., and Burchell M. J. 2008b. Sulfur mobilization in Stardust impact tracks. 39th Lunar and Planetary Science Conference. Abstract #1561. CD-ROM.

Keller L. P. and Messenger S. 2008. Relict amorphous silicates in Stardust samples (abstract). *Meteoritics & Planetary Science* 43: A74.

Noguchi T., Nakamura T., Okudaira K., Yano H., Sugita S., and Burchell M. J. 2007. Thermal alteration of hydrated minerals during hypervelocity capture to silica aerogel at the flyby speed of Stardust. *Meteoritics & Planetary Science* 42:357–372.

Nozaki W., Nakamura T., and Noguchi T. 2006. Bulk mineralogical changes of hydrous micrometeorites during low temperature heating in the upper atmosphere. *Meteoritics & Planetary Science* 41:1095–1114.

Stöffler D. 1972. Deformation and transformation of rock-forming minerals by natural and experimental shock processes. *Fortschritte der Minerogie* 49:50–113.

Trigo-Rodríguez J. M., Domínguez G., Burchell M. J., Hörz F., and Llorca J. 2008. Bulbous tracks arising from hypervelocity capture in aerogel. *Meteoritics & Planetary Science* 43:75–86.

Trucano T. G. and Grady D. E. 1995. Impact shock and penetration fragmentation in porous media. *International Journal of Impact Engineering* 17:861–872.

Tsou P. 1990. Intact capture of hypervelocity projectiles. *International Journal of Impact Engineering* 10:615–627.

Tsou P., Brownlee D. E., Sandford S.A., Hörz F., and Zolensky M. E. 2003. Wild 2 and interstellar sample collection and Earth return. *Journal of Geophysical Research* 108(E10), 8113:1–21.

Tsuchiyama A. and Iida Y. 2007. 3-D image analyses for so-called "spiral" tracks in C2017, 2,100,0 using X-ray microtomography, Informal Report to Stardust PE Team. 3 p.

Westphal A. J., Snead C., Butterworth A., Graham G. A., Bradley J. P., Bajt S., Grant P. G., Bench G., Brennan S., and Pianetta P. 2004. Aerogel keystones: Extraction of complete hypervelocity impact events from aerogel collectors. *Meteoritics & Planetary Science* 39:1375–1386.

Zolensky M. E., Zega T. J., Yano H., Wirick S., Westphal A. J., Weisberg M. K., Weber I., Warren J. L., Velbel M. A., Tsuchiyama A., Tsou P., Toppani A., Tomioka N., Tomeoka K., Teslich N., Taheri M., Susini J., Stroud R., Stephan T., Stadermann F. J., Snead C. J., Simon S. B., Simionovici A., See T. H., Robert F., Rietmeijer F. J. M., Rao W., Perronnet M. C., Papanastassiou D. A., Okudaira K., Ohsumi K., Ohnishi I., Nakamura-Messenger K., Nakamura T., Mostefaoui S., Mikouchi T., Meibom A., Matrajt G., Marcus M. A., Leroux H., Lemelle L., Lanzirotti A., Langenhorst F., Krot A. N., Keller L. P., Kearsley A. T., Joswiak D., Jacob D., Ishii H., Harvey R., Hagiya K., Grossman L., Grossman J. N., Graham G. A., Gounelle M., Gillet P., Genge M. J., Flynn G., Ferroir T., Fallon S., Ebel D. S., Dai Z. R., Cordier P., Clark B., Chi M., Butterworth A. L,. Brownlee D. E., Bridges J. C., Brennan S., Brearley A., Bradley J. P., Bleuet P., Bland P. A., and Bastien R. 2006. Mineralogy and petrology of comet Wild 2 nucleus samples. *Science* 314:1735–1739.